Stresses in the lunar interior: insights from slip directions in the A01 deep moonquake nest

Turner Alice R[1], Hawthorne Jessica Cleary[2], and Gaddes Matthew[3]

[1]University of Oxford
[2]Department of Earth Sciences, University of Oxford
[3]COMET

November 16, 2022

Abstract

We probe the present-day stresses in the lunar interior by examining the slip directions of moonquakes in the A01 nest. In this nest, some deep moonquakes appear to slip 'backwards', in the opposite direction to other events. We assess whether these changes in slip direction result from a spatial variation in the tectonic stress or from a temporal variation in the tidal stress. To test these two options, we first show that a dominant tectonic stress implies deep moonquakes can only slip in one direction: forwards and backwards, while a dominant tidal stress could allow moonquakes to slip in more directions: any combination of forwards, backwards, left, and right. Then we look for the number of slip directions; we separate the deep moonquake waveforms into slip directions using a principal component analysis technique. We find two slip directions present in the A01 deep moonquake nest. The moonquakes slip in a variety of directions as time evolves. This observation implies that the tidal stresses drive deep moonquakes. Additionally, these results place a new constraint on the magnitude of the tectonic stresses at depth; they must be smaller than the modelled tidal stress of ˜ 0.1 MPa.

Stresses in the lunar interior: insights from slip directions in the A01 deep moonquake nest

A. R. Turner [1], J.C. Hawthorne [1] and M. Gaddes [2]

[1]Department of Earth Sciences, University of Oxford, Oxford, UK
[2]COMET, University of Leeds, Leeds, UK

Key Points:

- We examine why some moonquakes appear to slip in the opposite direction from the others
- Using moonquake waveforms, we infer that slip direction changes through time because of tidal loading
- The results indicate that the tidal stress, with magnitude 0.1 MPa, is larger than the tectonic stress

Corresponding author: Alice Turner, alice.turner@earth.ox.ac.uk

Abstract

We probe the present-day stresses in the lunar interior by examining the slip directions of moonquakes in the A01 nest. In this nest, some deep moonquakes appear to slip "backwards", in the opposite direction to other events. We assess whether these changes in slip direction result from a spatial variation in the tectonic stress or from a temporal variation in the tidal stress. To test these two options, we first show that a dominant tectonic stress implies deep moonquakes can only slip in one direction: forwards and backwards, while a dominant tidal stress could allow moonquakes to slip in more directions: any combination of forwards, backwards, left, and right. Then we look for the number of slip directions; we separate the deep moonquake waveforms into slip directions using a principal component analysis technique. We find two slip directions present in the A01 deep moonquake nest. The moonquakes slip in a variety of directions as time evolves. This observation implies that the tidal stresses drive deep moonquakes. Additionally, these results place a new constraint on the magnitude of the tectonic stresses at depth; they must be smaller than the modelled tidal stress of ~ 0.1 MPa.

Plain Language Summary

The stresses that act in the lunar interior are not well known but are important for improving our knowledge of the interior of the Moon and its evolution. Deep inside the Moon, at depths between 700 km and 1200 km, moonquakes occur approximately every 27 days, suggesting they are influenced by the tides. Are the tides responsible for generating deep moonquakes? Or is long-term tectonic stress, in addition to the tidal stresses responsible? Using the waveforms of these deep moonquakes, we aim to determine the relative magnitudes of the tidal and tectonic stresses acting deep in the lunar interior. To do this, we look at the directions in which the moonquakes slip. We observe that deep moonquakes slip in a variety of different directions, which can only be caused by tidal stresses. Since these deep moonquakes are generated by the tides, this observation reveals that tectonic stresses in the lunar interior must be smaller than 0.1 MPa.

1 introduction

During the Apollo missions in the 1970s, four seismic stations were placed on the Moon's near side. These seismic stations recorded hundreds of deep moonquakes, which occur at depths of 700 - 1200 km.

Deep moonquakes tend to occur in clusters called "nests". In each nest, moonquakes occur at monthly intervals; they are seemingly influenced by the Earth-induced tidal stresses (Lammlein, 1977; Toksöz et al., 1977; Nakamura, 1978; Minshull & Goulty, 1988; Weber et al., 2009, 2010). However, the details of that influence remain unclear. Do tides trigger deep moonquakes by adding a small perturbation in stress on top of a large long-term tectonic stress? Or do tides generate deep moonquakes by providing most or all the stress at depth? Here we aim to resolve the role of tidal stresses in driving deep moonquakes and to constrain the relative magnitudes of tidal and tectonic stresses.

Some previous observations suggest that tidal stresses dominate the stress field in the deep moonquake source region. The tidal stress is large enough to account for the entire stress released in deep moonquakes (Kawamura et al., 2017). And large tidal stresses could also explain why some moonquakes appear to slip "backwards": in the opposite directions of most moonquakes in the nest. Moonquake slip directions could reverse if the tidal stresses dominate the local stress field and allow a reversal in the stress direction over their monthly oscillations (Toksöz et al., 1977; Nakamura, 1978).

However, other observations suggest that tectonic stresses dominate the local stress field. The tidal stresses may be larger than moonquake stress release, but local confining stresses are 10,000 times larger still (Minshull & Goulty, 1988). Additionally, deep moonquakes must respond to some non-tidal stress, as they do not always occur when the tangential tidal stress is the highest (Araki, 2001; Weber et al., 2009).

1.1 Motivation

1.1.1 Insights for the lunar interior

If tectonic stresses dominate the local stress field, they could have a variety of origins. They could be elastic stresses preserved from early lunar events (Weber et al., 2009); stresses generated by continuing weak convection (Frohlich & Nakamura, 2009); thermal stress from contraction of the lunar interior as it cools (Minshull & Goulty, 1988; Solomon & Chaiken, 1976); volumetric stresses from phase changes (Weber et al., 2009); or stresses concentrated around compositional heterogeneities within the lunar interior (Zhao et al., 2012; Qin et al., 2012; Sakamaki et al., 2010; Steinberger et al., 2015). There are, however, few observational constraints on the stresses involved in these processes (Solomon & Chaiken, 1976). We may better constrain the long term stress magnitudes by understanding the stresses that drive deep moonquakes.

1.1.2 Deep moonquake mechanisms

Understanding the stresses in the lunar interior may also help us understand deep moonquakes themselves. These ruptures are enigmatic; they occur at pressures of ~ 4 GPa and temperatures of 1500 to 1600 K (Kawamura et al., 2017), where rocks are expected to deform slowly and ductilely, not in abrupt brittle failures.

Three mechanisms are commonly proposed to explain the existence of deep moonquakes: the same mechanisms proposed to generate intermediate-depth (~ 100 km) and deep (> 410 km) earthquakes. Deep moonquakes may occur via (1) increased pore fluid pressure, which decreases the effective normal stress and allows for brittle failure at greater depths (e.g., Davies, 1999; Meade & Jeanloz, 1991; Hacker et al., 2003; Proctor & Hirth, 2015; Brantut et al., 2011; Dobson et al., 2002). Alternatively, they may occur via (2) thermal runaway, where a large initial shear stress and a small increase in strain rate lead to heating, runaway weakening and failure (e.g., Ogawa, 1987; Karato et al., 2001; Kelemen & Hirth, 2007; John et al., 2009; Thielmann et al., 2015; Thielmann, 2018). Or finally, moonquakes may occur via (3) a volume change and faulting associated with a mineralogical phase change (e.g., Kirby et al., 1996; Kirby, 1987; Green & Burnley, 1989; Burnley et al., 1991; Schubnel et al., 2013).

1.2 Models of reversed polarity moonquakes

In our search for the relative magnitudes of the tidal and tectonic stresses in the moonquake source region, we will focus on the stresses that allow reversed polarity moonquakes. Reversed polarity moonquakes generate waveforms similar to the waveforms of normal-polarity moonquakes, just flipped (Figure 1a). These reversed polarity waveforms were observed at the A01 deep moonquake nest in 1972, 1973 and 1974, interspersed with normal polarity waveforms (Nakamura, 1978). They originate from the same location as the normal polarity moonquakes but imply that some moonquakes in this location slip in the opposite direction to the rest. We test two models to explain this slip reversal.

1.2.1 Tectonic plug model

In the first proposed model, the long-term tectonic stress is larger than the oscillatory tidal stress. The shear stress at a given location is thus always in the same direction (arrows in Figure 1b). However, the stress may vary in space. Slip may occur on two parallel shear zones on either side of a moving plug, as sometimes observed during volcanic dyke intrusions (White et al., 2011). The motion of the plug would produce moonquakes that slip in roughly opposite directions, as observed.

1.2.2 Tidal model

In the second proposed model, first suggested by Nakamura (1978), the oscillatory tidal stress is larger than the long-term tectonic stress. The stress direction can thus vary with time on a fixed fault plane (Figure 1c). Reversed polarity moonquakes can occur on the same fault plane as normal moonquakes.

1.2.3 Differentiating between models for apparent slip reversal in the A01 nest

To test these models, we note that in the plug model, the stress is either forwards or backwards; there is one stress direction for each side of the plug. But in the tidal model, the stress can also rotate to different rakes along the fault plane (from the green to the blue arrow in Figure 1c). Since faults slip in the direction of the stress, we can make a similar statement about moonquake slip directions. In the plug model, moonquakes can slip forwards and backwards, but in the tidal model, moonquakes can slip in 2-D space, with any combination of left, right, forwards, and backwards.

We aim to determine whether the normal and reversed polarity moonquakes in the A01 nest slip along one direction (forwards and backwards) or along two directions (left, right, forwards, and backwards) and thus identify the dominant stress generating deep moonquakes. To do so, we will separate the energy in the deep moonquake waveforms into one or more slip directions with a principal component analysis (PCA) approach. We will apply a range of statistical tests to assess the slip directions' robustness.

2 Data Selection and Initial Processing

In this study, we focus on the A01 deep moonquake nest. The nest is located 18° southwest of station S12 at a depth of 870 km (Nakamura, 2005) and is the most active moonquake nest, providing enough good quality data to determine the number of slip directions.

We download the 3-component long period Apollo seismic data from the GEOSCOPE observatory through the IPGP data center (http://datacenter.ipgp.fr/). The original data was stored on magnetic tape, but it has been extracted from binary to SEED format for easier access (Nunn et al., 2017; Nunn, Weber, & Panning, 2020). The data were recorded in two instrument response modes, flat and peaked mode. The peaked instrument response mode was the natural response of the seismometer, with a peak in the frequency response at about 0.45 Hz (Nunn, Garcia, et al., 2020). The flat instrument mode was designed to be sensitive to a broader frequency range, from about 0.1 to 1 Hz (Nunn, Garcia, et al., 2020). We consider moonquakes recorded in the two instrumental modes and at each station separately, so we leave the data as they were recorded and do not deconvolve the instrument response.

To identify A01 moonquakes, we use the Nakamura (2003) catalogue with updates from Bulow et al. (2005). We assess the waveforms by eye to include only moonquakes with clear onsets and good signal to noise ratios.

We found few good quality moonquakes with clear arrivals at stations S14 or S15 and therefore analyse data from stations S12 and S16 only. Figure 2 illustrates the waveforms recorded in peaked mode on the north channel (MHN) of station S12. Figures s.1 - s.7 illustrate waveforms recorded on the east channel (MHE), in flat mode, and at station S16.

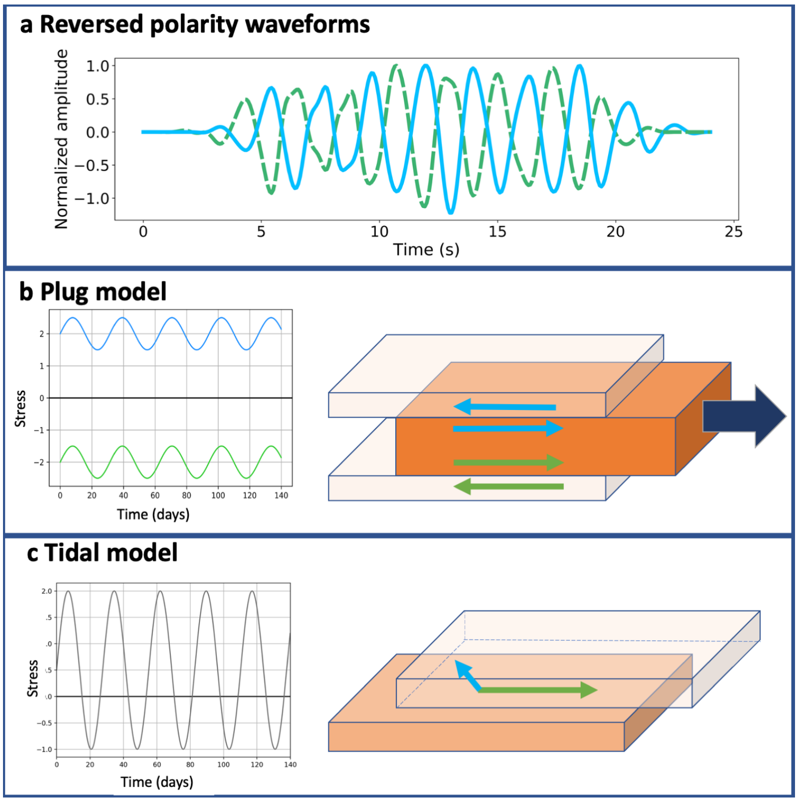

Figure 1. (a) A pair of moonquakes with reversed polarities, recorded on the east channel of station S16. The blue waveform was recorded on 17^{th} November 1973, and the green waveform was recorded on 5^{th} October 1975. Two models have been proposed to explain the reversed polarity waveforms. In (b) the plug model, the long-term tectonic stress is larger than the oscillatory tidal stress. The stress directions (arrows) are constant in time but change from one side of the plug to the other. In (c) the tidal model, the tidal stress is larger than the tectonic stress. Slip occurs on a single fault plane, and the stress direction (arrows) changes over time, assuming a range of rakes.

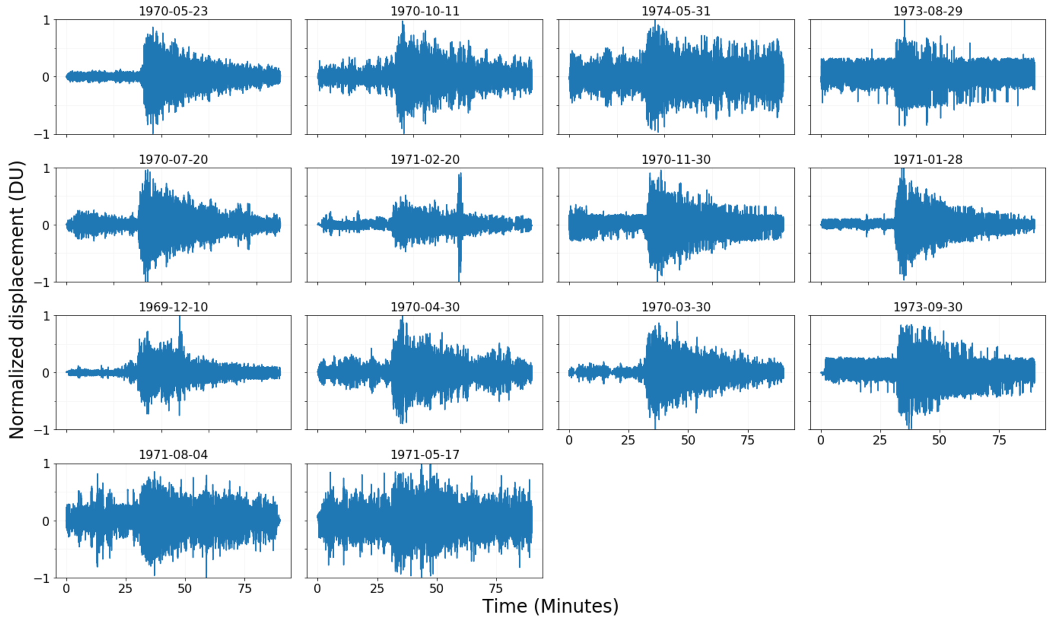

Figure 2. Deep moonquake waveforms used for PCA decomposition, recorded at station S12, channel MHN, in the peaked operation mode.

3 Principal component analysis of A01 moonquake waveforms

To assess the stress state in the deep moonquake generating region, we examine moonquake slip directions using a principal component analysis, a method not regularly used on earthquakes. For terrestrial problems, researchers often determine individual earthquake's focal mechanisms—their fault planes and slip directions—using the polarities of first arrivals recorded at a number of stations (e.g., Hardebeck & Shearer, 2002; Yang et al., 2012). However, moonquake slip directions cannot be estimated with those techniques; moonquake seismograms have emergent onsets, as shown in Figure 2 and are recorded at only four stations (Nakamura, 1978; Weber et al., 2009).

Instead, then, we determine the range of moonquake slip directions by comparing waveforms of various events in the A01 nest. Let us consider all the A01 moonquake seismograms $U_k(t)$ recorded on a single channel at a single station. Since the moonquakes in a nest occur within a compact cluster, only a few km wide (Nakamura, 1978), we can model the displacement at the lunar surface created by the moonquake as :

$$U_k(t) = \sum_{j=1}^{J} G_j(t) m_{jk}, \tag{1}$$

as illustrated in Figure 3. Here U_k is the waveform for event k, and G_j is the Green's function: the surface displacement produced by unit moment (slip times area times local shear modulus) in direction j. We call m_{jk} the slip coefficient: it is the moment in direction j for event k.

If we collect the waveforms $U_k(t)$ observed from several A01 moonquakes k into the columns of the matrix $\mathbf{U}$, we may note that Equation 1 has the same form as that used in the principal component analysis: $\mathbf{U} = \mathbf{G}\mathbf{m}$. PCA decomposes the data matrix ($\mathbf{U}$) into a set of coefficients (rows of $\mathbf{m}$) multiplied by a set of basis vectors or principal components (columns of $\mathbf{G}$). It would thus seem that we can use a PCA decomposition to recover the slip coefficients (m) and Green's functions (G) from the deep moonquake waveforms.

However, it is important to note that the PCA decomposition always recovers the same number of principal components as waveforms. The components are chosen such that the first components accommodate as much of the signal in the data vectors U_k as possible. Later components accommodate progressively less signal. We expect the first few principal components to be Green's functions for the slip in one or more directions, as they can accommodate signal from multiple moonquakes. Later principal components are likely to be noise, which differs from event to event. Our challenge will be to determine which principal components represent Green's functions and which principal components represent noise.

The number of principal components representing Green's functions will let us distinguish between the two models of moonquake slip presented in section 1.1. For the plug model, we hypothesise that there is a single slip direction; one direction should have a large m_1 and contain signal common to multiple moonquakes, while all other m_k should be close to zero. In contrast, the tidal model predicts two slip directions; two directions should have a large m_1 and m_2, and all other m_k should be close to zero.

In carrying out the PCA, we must ensure good waveform alignment. The signal in each principal component is sensitive to waveform alignment, as time-shifted traces can be mapped into different components. Before we compute the PCA decomposition, we cross-correlate each waveform with a high-quality template event to obtain a best-fitting initial time shift, as described in section 2. Then we apply the principal component analysis to a 10-minute window of the A01 deep moonquake waveforms, which includes the direct P and S arrivals and scattered arrivals in the coda. Finally, we ensure the best alignment between the waveforms by searching 0.7 s (10 samples) around the cross-correlation time shifts to maximise the energy in the first component of the PCA.

The Green's functions determined from the PCA decomposition are plotted in Figure 4. We discuss their qualitative characters in section 4. In section 5, we examine the slip coefficients and principal components more quantitatively.

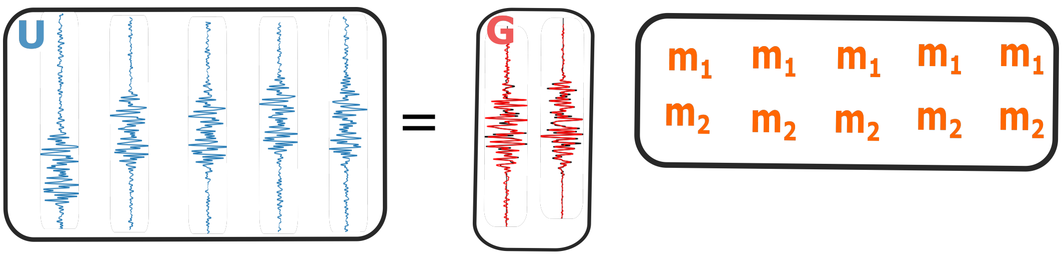

Figure 3. Illustration of the PCA decomposition for the A01 moonquakes into two slip directions. A matrix of waveforms (blue, **U**), is decomposed into the Green's Functions (red, **G**), and the slip coefficients (orange, **m**) for each of the two slip directions illustrated. The later components also recovered in the PCA are not illustrated.

4 Qualitative analysis of the principal components (G)

Figure 4 shows the 14 principal components for the peaked mode MHN records at station S12, ordered by the percentage of the data variance they explain. The first three principal components, which explain the most variance, have clear onsets in signal followed by decays. They have "moonquake-like" shapes, similar to the waveforms in Fig-

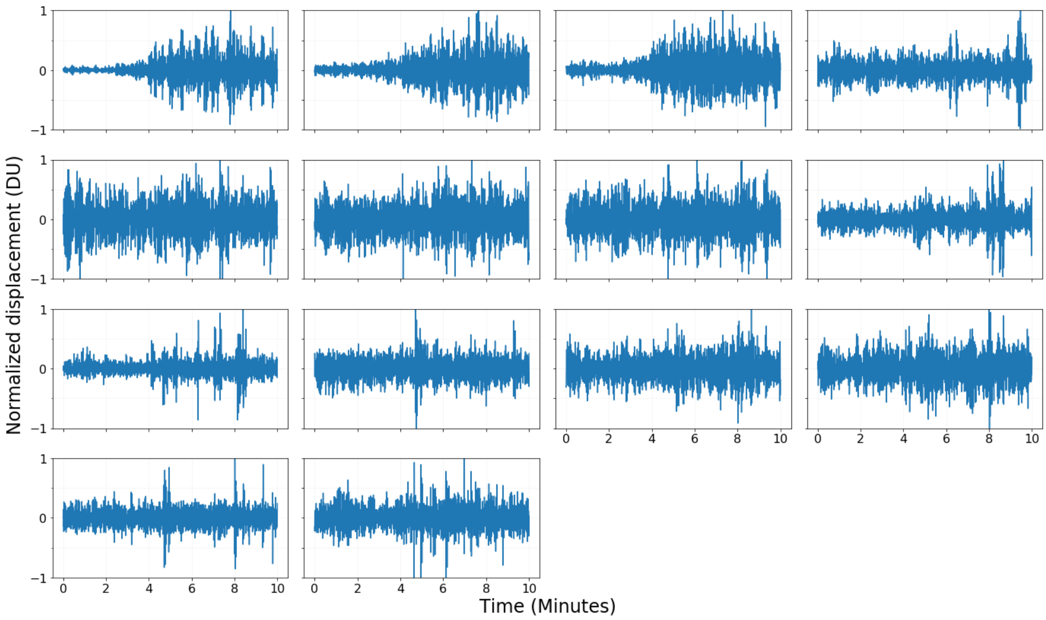

Figure 4. Principal components derived from the S12 MHN data in the peaked operational mode of the instrument.

ure 2. These shapes suggest that the first three principal components could represent real Green's functions. Later principal components, which explain progressively less of the variance, do not have clear onsets or decaying "moonquake-like" shapes.

Using the MHE records at station S12 (Figure s.8), we also observe three moonquake-shaped principal components. However, when we analyse the flat mode MHN and MHE data (Figures s.9 and s.10), there are only two "moonquake-shaped" principal components.

When we analyse the waveforms recorded at station S16 (Figures s.11 - s.14), we again observe three moonquake-shaped components in the decomposition of the peaked mode data and two moonquake-shaped components in the flat mode data. A qualitative analysis of all the data thus suggests that two or three principal components represent Green's functions, while the rest represent noise.

5 Quantitative analysis of the number of slip directions

Next, we aim to more rigorously determine whether each derived principal component represents a Green's function or represents noise. We quantitatively analyse the "slip" coefficients m obtained for each principal component and event (section 5.1) as well as the principal component vectors G themselves (section 5.2).

5.1 Determining number of slip directions using unbiased principal component coefficients (m')

The "slip" coefficients m_{jk} determine how much of each principal component j is needed to reconstruct the seismogram generated by moonquake k. If a principal component $G_j(t)$ represents a real Green's function, its coefficients are likely to be large for multiple moonquakes k. We therefore aim to assess the coefficients' values.

To accurately assess the coefficients' values, we need to compare the principal component vectors with "unseen" validation waveforms. We want to know how well each principal component can be used to reconstruct moonquake waveforms that were not employed in creating the principal component vectors.

To achieve this, we use a method similar to "leave-one-out cross-validation" (Bishop & Nasrabadi, 2006). We calculate the PCA using all but one "left-out" moonquake waveform. We project the left-out waveform onto each of the principal components to obtain an unbiased coefficient m'_{jk} for component j and moonquake k:

$$m'_{jk} = G_{res,j}(t) \bullet u_k(t). \tag{2}$$

Here u_k is the waveform of the excluded moonquake, and $G_{res}j$ is the jth principal component, calculated using the remaining moonquakes. We repeat this process, excluding each available moonquake k in turn, so that we have a set of unbiased coefficients m'_{jk} for each moonquake.

We use a bootstrap approach to estimate the uncertainty on the coefficients m'_{jk}. We again exclude event k and recompute the principal components, but instead of using all remaining moonquakes in the PCA calculation, we randomly choose 20 of the remaining moonquakes with replacement. With this new subset of moonquakes, we recompute the principal components $G_{res,j}$ and the projected coefficients m'_{jk} 25 times.

The coloured circles in Figure 5b-d show these 25 projected coefficients m'_{jk} for each of the station S12 MHN moonquakes. The coefficient for the first principal component m'_{i1} is plotted on the x-axis. The coefficients of the second (m'_2), third (m'_3), and twentieth (m'_{20}) principal components are plotted on the y axis of panels b,c and d, respectively. Each event k is plotted in a different colour.

Figure 5a summarises the distribution of the coefficients of the first principal component m_1 for all moonquakes from the peaked mode S12 data. The distribution of the coefficients is bi-modal, with clusters around ± 12. Note that a single event can have both a positive and negative m' because the signs of G_i and m'_i can trade-off; in bootstrapping, G_i can flip and be compensated by a flip in the sign of m'_i. The non-zero average amplitude of the coefficients, along with the gap around zero, implies that there is a large m'_1 common to all moonquakes. The first principal component thus seems to represent a real Green's function.

Panel e summarises the distribution of the coefficients of the second principal component, m'_2. The bi-modal distribution and non-zero average amplitude of the coefficients that imply the second principal component also represents a real Green's function.

Panel f and g summarise the distribution of coefficients for the third and twentieth components. These distributions have only a single peak, and the average values of the distributions are near zero. The near-zero values suggest that there is little moonquake signal in these principle components; they mostly accommodate noise that varies from event to event.

We may more quantitatively compare the coefficient distributions with a Kolmogorov-Smirnov test. We assume that the last (twentieth) principal component accommodates only noise, and take its coefficient distribution, plotted in panel g, as representative of the coefficients derived from noise. The first and second principal components' coefficients differ from this noise distribution with probabilities of near 100% and 99.1%, respectively; these coefficients likely accommodate moonquake signals. In this analysis of the peaked mode S12 data, the third component's coefficients differ from the noise with a probability of only 30%. Later components' coefficients are also similar to the distribution of noise.

We obtain similar results when we analyse the distribution of coefficients for all other stations, components, and instrument modes. For example, Figure s.15 summarises the distribution of coefficients for the station 12 peaked mode MHE waveforms. The distributions of coefficients for the first and second principal components are again bi-modal, and the average distribution amplitude is non-zero. The distributions differ from noise with probability near 100 % and 99 %, respectively. The distribution of coefficients in the third and later slip directions have only a single peak at zero and are similar to the distribution of coefficients derived from noise.

Similar although slightly less well-resolved distributions are obtained from flat mode data at station S12 (Figure s.16 and s.17). For both the MHN and MHE records, the distributions of coefficients for the first principal components are bi-modal, and both differ from noise with probabilities near 100 %. The distributions of the second principal components are not bi-modal, but they are uniform rather than Gaussian. The distributions still differ from the noise distributions with a probability of 92% and99% for the MHN and MHE records. The third principal component also differs from noise with a probability of 99 %, but it has a large peak at zero. Later components are similar to noise.

Similar results are obtained from station S16, as illustrated in Figures s.18 - s.21. The distributions from all stations and channels imply that two principal components have a large m'_{jk} common to multiple moonquakes and represent real slip directions.

5.2 Determining number of slip directions using the similarity of the principal component vectors (G)

In the bootstrapping described above, we re-estimated the principal components G_j and coefficients m'_j for various subsets of the data, and we analysed the coefficients m'_j. In this section, we examine the variation among the estimated principal component vectors G_j.

We expect little variation in the estimates of a given principal component G_j if that component recovers a real moonquake signal common to multiple moonquake waveforms. But we expect large variation in bootstrapped estimates of a principal component G_j if that principle component recovers noise, which varies between waveforms.

We examine the similarity of the bootstrapped principal components using a modified version of the algorithm ICASAR. This algorithm was originally designed to separate ground deformation and atmospheric signals in time series of interferograms using independent component analysis (Gaddes et al., 2019), but we use it to analyse the similarity of our bootstrapped principal component estimates. The similarity between two principal component estimates is quantified as the absolute value of their cross-correlations.

The ICASAR algorithm clusters the bootstrapped principal components according to these cross-correlation values. It uses a hierarchical clustering algorithm (HBDSCAN) to identify similar principal component estimates (McInnes et al., 2017; Gaddes et al., 2019). We assess the quality of clusters using the cluster quality factor I_q: the difference between the mean intra-cluster similarity (1 for a perfect cluster) and the mean similarity between members of the cluster and all other component estimates (0 for a perfect cluster).

We would now like to visualise the similarities between the principal component estimates, but without plotting the numerous computed cross-correlations. To do so, we project the set of cross-correlations into a two-dimensional space. We choose the dimension's directions according to a t-distributed neighbourhood embedding algorithm. These directions do not have any physical meaning, but they preserve a key feature of distance: points close together represent component estimates that have a high cross-correlation,

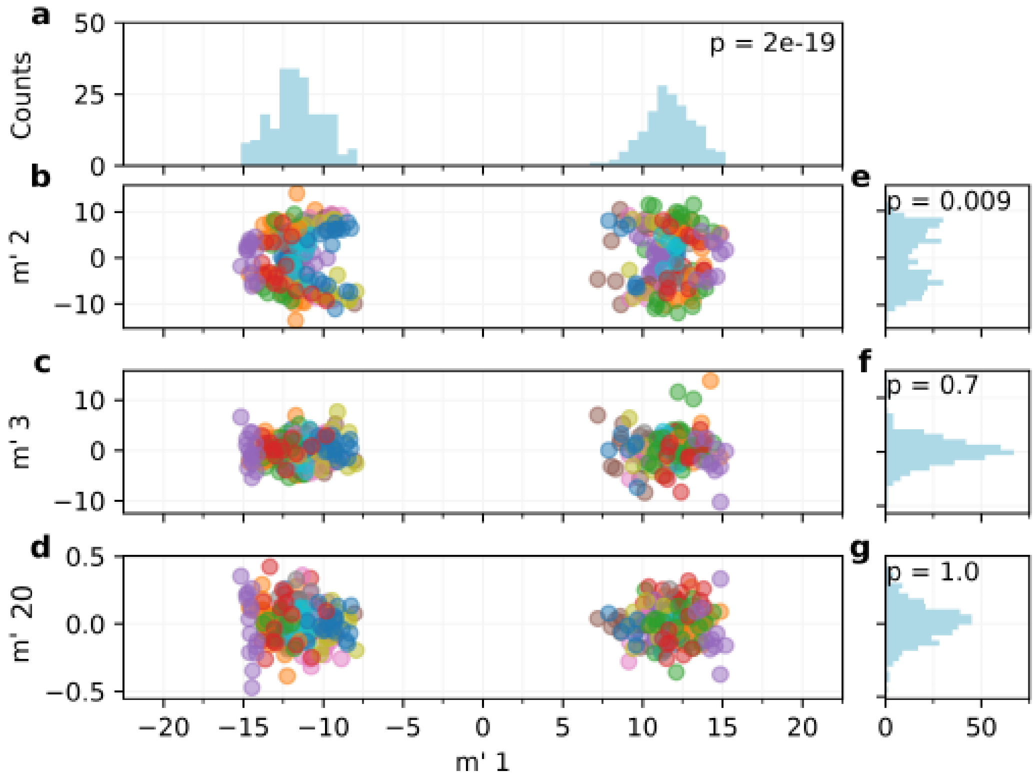

Figure 5. Unbiased coefficients of the principal components, from the S12 MHN data in the peaked operational mode. In panels b-d, the coefficient for the first principal component m'_{i1} is plotted on the x-axis. The coefficients of the second (m'_2), third (m'_3) and twentieth (m'_{20}) principal components are plotted on the y axis of panels b,c and d, respectively. Each event is plotted in a different colour. Panels a, e, f, and g summarise the distribution of coefficients for each of the principal components. The text in the top of panels a, e, f, and g is the probability (p-value) that each distribution differs from the distribution of the coefficients derived from noise. Only the first two components differ from noise.

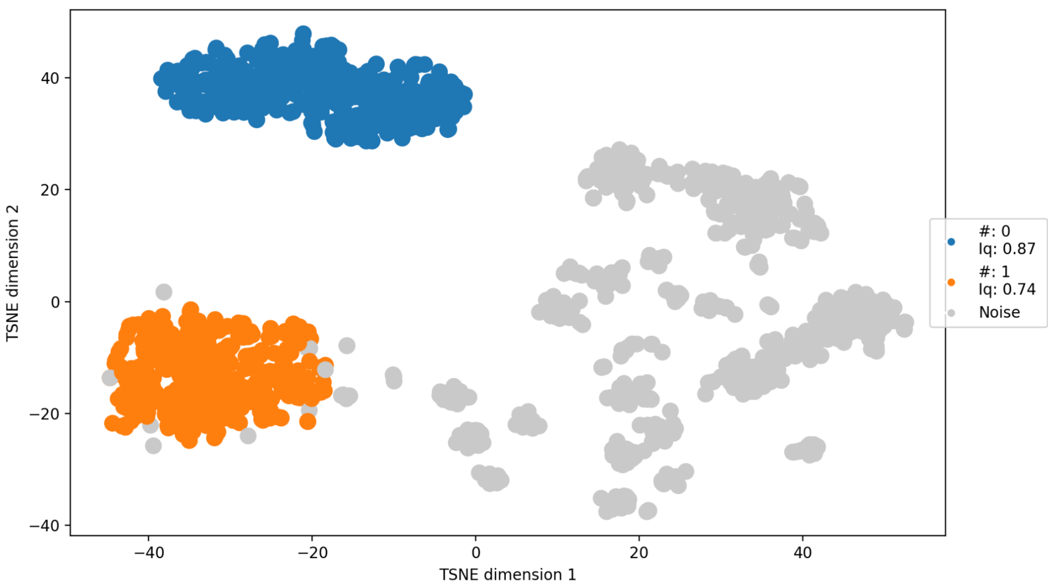

Figure 6. Clustering results of bootstrapped principal component vectors **G**, obtained for S12 MHN in peaked operational mode. One point is plotted for each bootstrapped estimate of a principal component, but only the first four principal components are plotted. The location of each point is determined by the t-sne algorithm, preserving the similarity of components from the higher dimensional space (Maaten & Hinton, 2008; Gaddes et al., 2019). The colour of each point is determined by the HBDSCAN clustering algorithm (McInnes et al., 2017; Gaddes et al., 2019). Two clusters are shown, in blue and orange. Grey points represent component estimates that are not assigned to a cluster.

while points that are far apart have a low cross-correlation (t-sne, Maaten & Hinton, 2008; Gaddes et al., 2019).

Figure 6 shows the clusters determined using principal components of waveforms recorded at station S12 MHN in peaked mode, projected along the first two t-sne directions. Only projections from the first four principal components are shown. Points in Figure 6 are coloured by the clusters identified by the HBDSCAN algorithm. The principal components estimates in the blue cluster are similar; they have an I_q of 0.87. The estimates in the orange cluster have a slightly lower similarity; $I_q = 0.74$. Points coloured grey represent principal component estimates that are not similar enough to other estimates to form a cluster.

The two clusters identified by the HBDSCAN algorithm and shown visually in Figure 6 suggest that two principal components contain signal common to multiple moonquakes and that these signals are repeatedly recovered in bootstrapping. We obtain similar clusters if we adjust the clustering parameters: if we perturb the minimum cluster size or the distance required to define a “neighbour”. Similar clusters are obtained from other stations, components, and instrument modes (Figures s.22-28).

5.3 Partitioning of slip between directions

Our analysis in sections 5.1 and 5.2 implies that moonquakes in the A01 slip in two directions. We can now analyse the magnitude of slip in each direction, as we can now interpret the first two coefficients m' not just as coefficients of principal components but

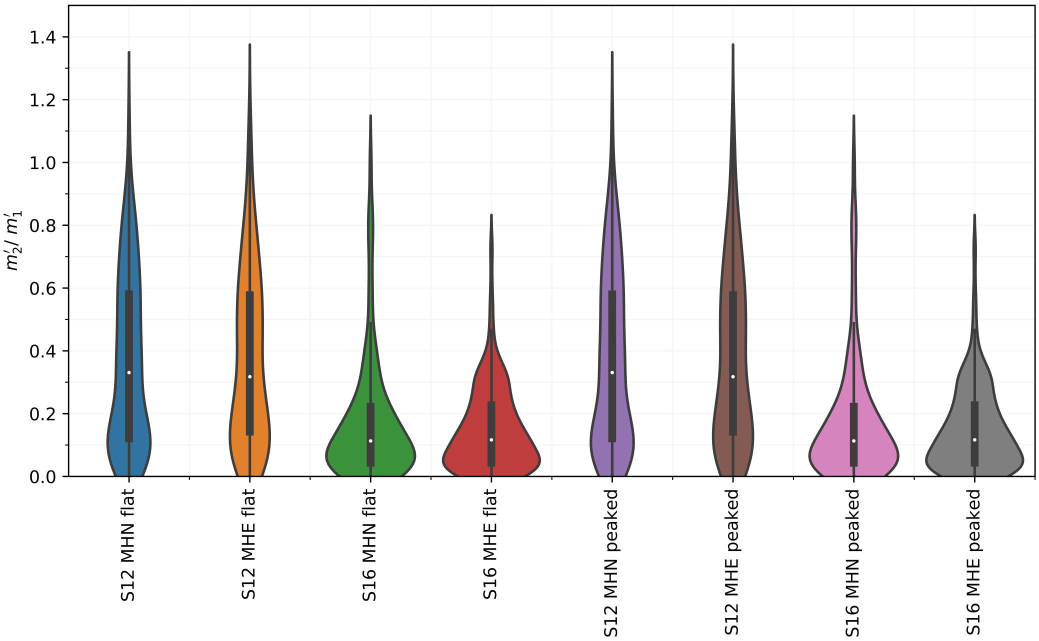

Figure 7. Slip coefficient ratio m_2'/m_1' for each station and channel. The white dot marks the median bootstrapped ratio at each station, the black bar delimits the interquartile range, and the thin black line delimits 1.5 $\times$ the inter-quartile range. The coloured areas illustrate the probability density of the ratio at each station. All distributions have peaks above zero, and the median m_2'/m_1' ratios range from 0.11 to 0.33.

as slip coefficients. Each m_{jk}' is proportional to the amount of moment in each direction for moonquake k.

Figure 7 shows distributions of the $|m_{1k}'/m_{2k}'|$ ratios: the ratio of the moment the second slip direction to the moment in the first slip direction. These distributions are also shown plotted on log axis in Figure s.29. The coloured area shows the probability density of the ratio obtained at each station and component, and the white dots mark the median ratio. All distributions are consistent with significant slip in the second direction; distributions have peaks above, not at zero, and the median ratios range from 0.11 to 0.33, with a median at all stations of 0.21 .

Finally, we can examine how the slip coefficients vary from moonquake to moonquake. Figure 8 shows the normalised $m_i'/\sqrt{m_1'^2 + m_2'^2}$ values for peaked mode MHN and MHE records at stations S12 and S16. If these recovered directions were orthogonal, a vector from the origin to each point would give the slip direction. Note, however, that our PCA analysis cannot identify orthogonal slip directions. It only identifies slip directions that produce different Green's functions, and those directions are the ones illustrated on the axes of Figure 8.

We can nevertheless interpret several features of the varying slip coefficients. First, Figure 8 shows both positive and negative coefficients in the first slip direction. The negative coefficients correspond to moonquakes that slip in the opposite direction of most events; they create the reversed polarity waveforms. Second, and perhaps more interesting, the slip directions do not appear clustered; there is a variable amount of slip in the second direction. Moonquakes appear to slip in a range of directions within a 2-D plane, not in two particular directions.

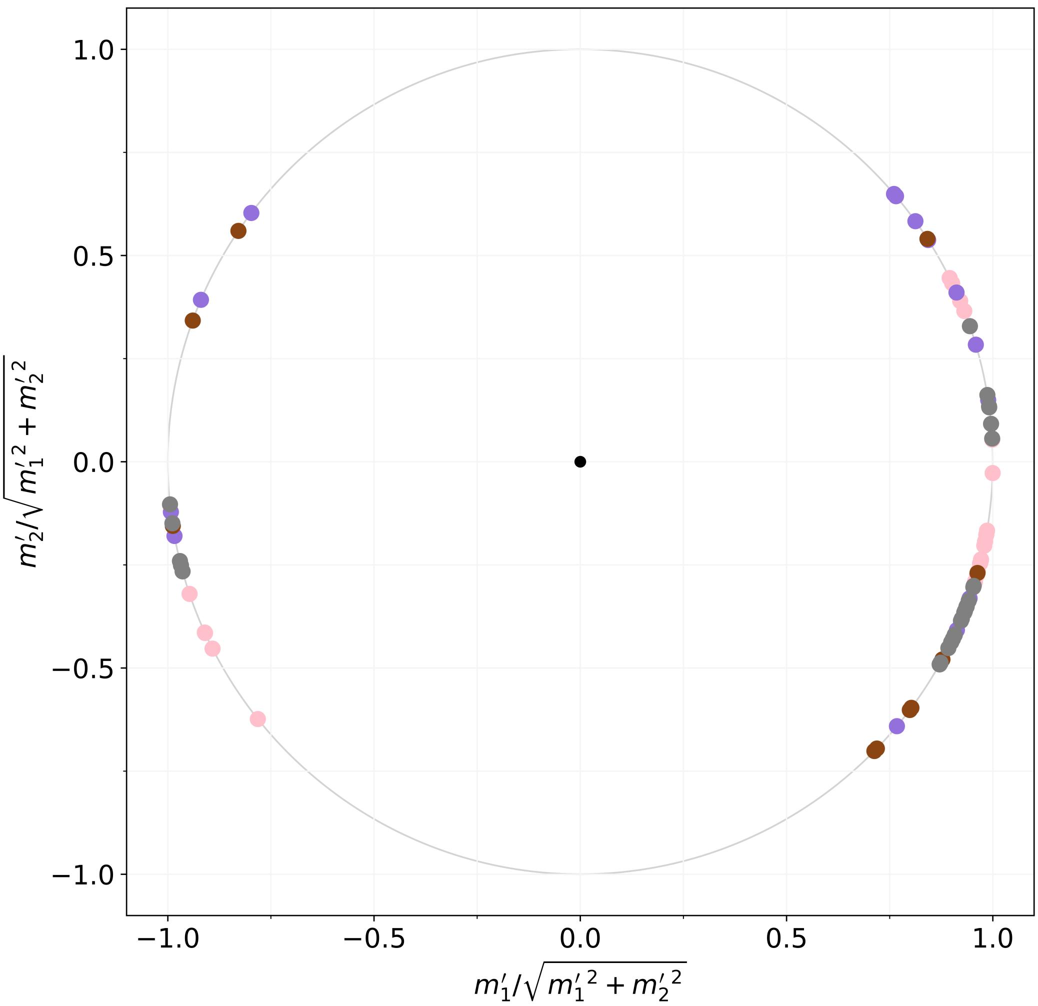

Figure 8. Normalised unbiased slip coefficients for the first and second Green's functions, for moonquakes recorded at both stations and components in the peaked instrument mode. A vector from each point to the origin would give the slip direction. Negative coefficients in the first slip direction correspond to reversed polarity moonquakes, which slip roughly in the opposite direction of most events. Note, however, that moonquakes appear to slip in a range of direction within the m_1-m_2 plane. The colours correspond to the station and channel considered, as used in Figure 7 (purple: S12 MHN peaked; brown: S12 MHE peaked; pink: S16 MHN peaked; grey: S16 MHE peaked).

6 Validation

Our analysis implies that two principal components are required to accommodate signal common to many moonquakes in the A01 nest: that these moonquakes slip in two directions. However, some errors have the potential to create artificial principal components. So here we check that the second significant principal component is a physical feature of the moonquakes and not a result of poor waveform alignment (section 6.1) or scattered seismic waves (section 6.2).

6.1 Potential influence of waveform alignment

We first check that we have not obtained two principal components because the moonquake waveforms are poorly aligned. We verify that the second principal component is not a time-shifted version of the first component. Then we examine how the number of significant principal components changes if we add errors in the waveform alignment: if we randomly shift each waveform by a random value drawn from a uniform distribution.

Figure 9 shows the percentage of the variance accommodated by the principal components as we increase the maximum random shift from 0 to 1 second. For shifts up to ~ 0.17 seconds, energy in the first principal component decreases as the alignment worsens, but that energy is distributed over a number of the later components; the energy in the second principal component does not increase significantly. Since our fine-tuning of the time-shift allows an accuracy of 0.07 seconds (the sampling rate of the traces), it seems unlikely that the significant energy we observe in the second principal component results from poor waveform alignment.

6.2 Potential influence of scattering

Next, we assess whether the second slip direction could result from scattering. Moonquakes in the A01 may be in slightly different locations, up to a few km of each other (Nakamura, 2003), and their seismic waves may follow slightly different paths through the Moon, especially in the near-surface scattering layer. The different paths could lead to different recorded seismograms, especially later in the coda, when the seismic waves have been more scattered.

To look for scattering, we apply the PCA to 30-second windows throughout the seismogram, from the direct S wave arrival onward into the coda, as illustrated in Figure 10a. Figure 10b shows the variance explained by the first, second, and twentieth principal components in each of the windows. The different operational modes, components, and stations also give similar results. The variance in the second component does not significantly increase later in the coda, suggesting that scattering later in the coda does not create the significant signal we observe in the second principal component.

7 Discussion

In this study, we have used a PCA approach to separate the signal in deep moonquake waveforms into principal components common to multiple moonquakes. We find that two principal components are required to reconstruct the data. These components likely reflect the signals created by slip in two different directions.

7.1 Explaining reversed polarity moonquakes

We were motivated to examine moonquake slip directions because some moonquakes have reversed polarity waveforms; these moonquakes appear to slip “backwards”. We sought to determine whether this reversal arises because of a spatially varying tectonic

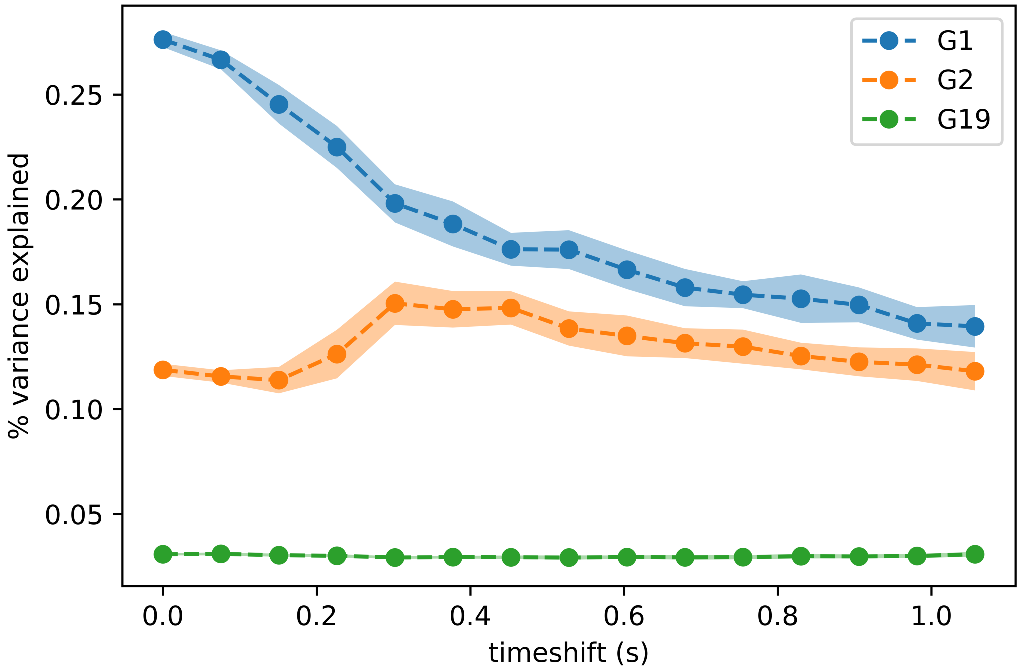

Figure 9. Testing the influence of inaccurate waveform alignment. We apply random timeshifts with magnitude up to 1.1s (x-axis) and determine the percentage of the data variance explained by the first (blue), second (orange), and nineteenth (green) principal components.

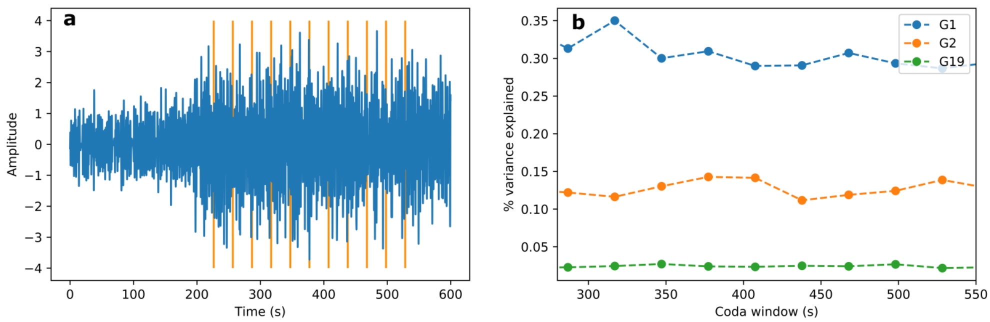

Figure 10. a) A single moonquake waveform, observed at station S12 in flat mode, divided (orange lines) into 30s windows throughout the coda, starting after the high-amplitude S wave arrival. b) Percentage variance accommodated by the first, second and last components in each time window. The variance percentages remain roughly constant as we move from the direct arrival into the more scattered coda. Scattering thus does not appear to explain the significant signal in the second component.

stress, where stress changes direction on either side of a plug (Figure 1b), or whether the reversal arises because the tectonic stress is small, and a tidal stress drives moonquakes and changes direction through time (Figure 1c). To distinguish between these models, we note that the tectonically driven plug model implies only one slip direction: forwards or backwards, while the tidal stress model could allow two slip directions: any combination of forwards, backwards, left, or right. Our observation of two slip directions is more consistent with the tidal model of reversed polarity waveforms.

In principle, however, the plug model could also allow two slip directions. If the two sides of the plug are not parallel, we might see one slip direction (A) on one side of the plug and another direction (B) on the other side. In this case though, the two slip directions would be fixed. Slip might occur in direction A and in direction B, but not in any direction along the plane that contains directions A and B. For such a scenario, we could expect the estimated slip coefficient vectors, $[m_1, m_2]$, as decomposed using principal component analysis, to cluster around two directions, representing slip directions A and B on either side of the plug. We do not observe that clustering.

Instead, we see variation in the first and second slip coefficients (Figure 8). That 2-D variation is more consistent with the tidal model, which allows the slip direction to move along the fault plane as the tidal stress changes.

The variation in the slip direction we observe is also consistent with P/S amplitude variations (Nakamura, 1978) and changes in the slip direction determined from S wave polarities (Koyama & Nakamura, 1980), all of which suggest slip occurs on a fixed fault plane, but the direction of slip can vary with time.

The two slip directions we identify thus suggest that an oscillating tidal stress drives deep moonquakes in the A01 nest and that this tidal stress changes the local stress direction through time.

7.2 Implications of a small tectonic stress

If tidal loading changes the direction of stress in the moonquake region through time, the tidal stresses must be larger than the local tectonic stress. We thus have a new constraint on the magnitude of the tectonic stress at depth; it must be less than the maximum modelled tidal stress of ~ 0.1 MPa (Toksöz et al., 1977; Minshull & Goulty, 1988; Weber et al., 2009).

7.2.1 Excluding a ductile mechanism for moonquakes?

We may use this cap on the tectonic stress to help constrain the enigmatic mechanism of deep moonquakes under high pressures and temperatures. Some models have suggested that moonquake slip is driven by a viscous thermal runaway (Thielmann et al., 2015). As the fault slips, the temperature increases, grains reduce in size, and melting can occur, localising and accelerating the slip on the fault. The runaway process allows ductile failure on seismic timescales. However, large initial shear stresses (~ 100 MPa at high strain rates (Thielmann et al., 2015)) are required to initialise localisation, and those stresses are not compatible with our 0.1 MPa upper bound on the tidal and tectonic stress in the A01 moonquake region. This allows us to rule out this mechanism for deep moonquakes.

A variety of models remain to explain the rapid failure that creates moonquakes at high pressure and temperature, though all the models remain poorly tested. One model suggests that high pore fluid pressure could reduce the effective stress on faults at depth and enable deep moonquake faults to slip. The lunar interior is wetter than previously thought (Evans et al., 2014). However, it remains unclear whether there is enough water in the right places to account for the generation of deep moonquakes.

Alternatively, deep moonquakes could be related to a mineral phase change, as proposed for deep (> 400 km) earthquakes. However, current models of the lunar interior do not identify a suitable phase change (Garcia et al., 2012), and this phase change would have to somehow occur repeatedly to create repeating moonquakes in a small volume.

7.2.2 Lunar interior

In addition to improving our understating of the mechanism of deep moonquakes, our moonquake-derived stress bounds, which imply that the local tectonic stress is smaller than the tidal stress, also provide constraints on thermal and dynamic models of the lunar interior. This stress bound implies that any stress from thermal contraction must be less than 0.1 MPa, consistent with previous estimates (Solomon & Chaiken, 1976). We can also place an upper bound on any remaining convection. If we assume a Newtonian viscosity of 10^{21} Pa s (e.g., Li et al., 2019), a long term stress smaller the 0.1 MPa implies a local strain rate smaller than 10^{-16} s^{-1}. Future research may find other uses for our moonquake-derived stress bounds. For example, the bounds might be used to provide constraints on stress concentrations around local heterogeneity within the lunar interior (Zhao et al., 2012; Qin et al., 2012; Sakamaki et al., 2010; Steinberger et al., 2015).

7.3 Further application to moonquakes and earthquakes

The methodology developed in this study may also be relevant for future work. We have applied the PCA methodology only to the A01 nest, but this technique could let us examine more moonquakes, as recorded in the Apollo data or in data collected by the new broadband seismometer on the Farside Seismic Suite package, expected to land on the far side of the Moon in 2024 or 2025.

The PCA method appears necessary on the Moon, but it could also be useful for events on Earth, particularly in situations where there is no clear first arrival or where network coverage is sparse.

8 Conclusion

In this work, we sought both to understand the origin of moonquakes that slip "backwards" and to constrain the relative magnitudes of tidal and tectonic stresses deep in the lunar interior. Our observation of two slip directions implies that moonquakes' reversed polarity waveforms result from an oscillating tidal stress, which encourages moonquakes to slip forwards, backwards, left, or right depending on the phase of the tide. To explain these varying slip directions, the tidal stresses, which have a magnitude around 0.1 MPa (Toksöz et al., 1977; Minshull & Goulty, 1988; Weber et al., 2009), must be larger than the local tectonic stress. Our observations thus imply that the tectonic stress near the A01 nest, at 900 km depth, is less than 0.1 MPa. That small tectonic stress may be employed in future modelling of the lunar interior. Further, the small stress implies that viscous thermal runaway, which requires a large stress for initiation (Thielmann et al., 2015), is unlikely to explain the existence of deep moonquakes.

Acknowledgments
We gratefully acknowledge the availability of the long period Apollo seismic data from the IPGP data centre (http://datacenter.ipgp.fr/data.php). We would like to thank Ceri Nunn and Taichi Kawamura for their useful insights on the Apollo seismic data. AT was supported by STFC studentship ST/S505626/1.

References

Araki, H. (2001). Focal processes of deep moonquakes. *Journal of the Geodetic Society of Japan*, *47*(1), 508–513.

Bishop, C. M., & Nasrabadi, N. M. (2006). *Pattern recognition and machine learning* (Vol. 4) (No. 4). Springer.

Brantut, N., Sulem, J., & Schubnel, A. (2011). Effect of dehydration reactions on earthquake nucleation: Stable sliding, slow transients, and unstable slip. *Journal of Geophysical Research: Solid Earth*, *116*(B5).

Bulow, R., Johnson, C., & Shearer, P. (2005). New events discovered in the apollo lunar seismic data. *Journal of Geophysical Research: Planets*, *110*(E10).

Burnley, P. C., Green, H. W., & Prior, D. J. (1991). Faulting associated with the olivine to spinel transformation in mg2geo4 and its implications for deep-focus earthquakes. *Journal of Geophysical Research: Solid Earth*, *96*(B1), 425–443.

Davies, J. H. (1999). The role of hydraulic fractures and intermediate depth earthquakes in subduction zone magmatism. *Nature*, *398*(6723), 142–145.

Dobson, D., Meredith, P., & Boon, S. (2002). Microseismicity associated with antigorite dehydration: Laboratorysimulation of deep-focus earthquakes. In *Egs general assembly conference abstracts* (p. 3985).

Evans, A., Zuber, M., Weiss, B., & Tikoo, S. (2014). A wet, heterogeneous lunar interior: Lower mantle and core dynamo evolution. *Journal of Geophysical Research: Planets*, *119*(5), 1061–1077.

Frohlich, C., & Nakamura, Y. (2009). The physical mechanisms of deep moonquakes and intermediate-depth earthquakes: How similar and how different? *Physics of the Earth and Planetary Interiors*, *173*(3-4), 365–374.

Gaddes, M., Hooper, A., & Bagnardi, M. (2019). Using machine learning to automatically detect volcanic unrest in a time series of interferograms. *Journal of Geophysical Research: Solid Earth*, *124*(11), 12304–12322.

Garcia, R. F., Gagnepain-Beyneix, J., Chevrot, S., & Lognonné, P. (2012). Erratum to "very preliminary reference moon model", by rf garcia, j. gagnepain-beyneix, s. chevrot, p. lognonné [phys. earth planet. inter. 188 (2011) 96–113]. *Physics of the Earth and Planetary Interiors*, *202*, 89–91.

Green, H., & Burnley, P. (1989). A new self-organizing mechanism for deep-focus earthquakes. *Nature*, *341*(6244), 733–737.

Hacker, B. R., Peacock, S. M., Abers, G. A., & Holloway, S. D. (2003). Subduction factory 2. are intermediate-depth earthquakes in subducting slabs linked to metamorphic dehydration reactions? *Journal of Geophysical Research: Solid Earth*, *108*(B1).

Hardebeck, J. L., & Shearer, P. M. (2002). A new method for determining first-motion focal mechanisms. *Bulletin of the Seismological Society of America*, *92*(6), 2264–2276.

John, T., Medvedev, S., Rüpke, L. H., Andersen, T. B., Podladchikov, Y. Y., & Austrheim, H. (2009). Generation of intermediate-depth earthquakes by self-localizing thermal runaway. *Nature Geoscience*, *2*(2), 137–140.

Karato, S.-i., Riedel, M. R., & Yuen, D. A. (2001). Rheological structure and deformation of subducted slabs in the mantle transition zone: implications for mantle circulation and deep earthquakes. *Physics of the Earth and Planetary Interiors*, *127*(1-4), 83–108.

Kawamura, T., Lognonné, P., Nishikawa, Y., & Tanaka, S. (2017). Evaluation of deep moonquake source parameters: Implication for fault characteristics and thermal state. *Journal of Geophysical Research: Planets*, *122*(7), 1487–1504. doi: 10.1002/2016JE005147

Kelemen, P. B., & Hirth, G. (2007). A periodic shear-heating mechanism for intermediate-depth earthquakes in the mantle. *Nature*, *446*(7137), 787–790.

Kirby, S. H. (1987). Localized polymorphic phase transformations in high-pressure faults and applications to the physical mechanism of deep earthquakes. *Journal* *of Geophysical Research: Solid Earth*, *92*(B13), 13789–13800.

Kirby, S. H., Stein, S., Okal, E. A., & Rubie, D. C. (1996). Metastable mantle phase transformations and deep earthquakes in subducting oceanic lithosphere. *Reviews of geophysics*, *34*(2), 261–306.

Koyama, J., & Nakamura, Y. (1980). Focal mechanism of deep moonquakes. In *Lunar and planetary science conference proceedings* (Vol. 11, pp. 1855–1865).

Lammlein, D. R. (1977). Lunar seismicity and tectonics. *Physics of the Earth and Planetary Interiors*, *14*(3), 224–273.

Li, H., Zhang, N., Liang, Y., Wu, B., Dygert, N. J., Huang, J., & Parmentier, E. (2019). Lunar cumulate mantle overturn: A model constrained by ilmenite rheology. *Journal of Geophysical Research: Planets*, *124*(5), 1357–1378.

Maaten, L. v. d., & Hinton, G. (2008). Visualizing data using t-sne. *Journal of machine learning research*, *9*(Nov), 2579–2605.

McInnes, L., Healy, J., & Astels, S. (2017). hdbscan: Hierarchical density based clustering. *J. Open Source Softw.*, *2*(11), 205.

Meade, C., & Jeanloz, R. (1991). Deep-focus earthquakes and recycling of water into the earth's mantle. *Science*, *252*(5002), 68–72.

Minshull, T., & Goulty, N. (1988). The influence of tidal stresses on deep moonquake activity. *Physics of the earth and planetary interiors*, *52*(1-2), 41–55.

Nakamura, Y. (1978). A1 moonquakes-source distribution and mechanism. In *Lunar and planetary science conference proceedings* (Vol. 9, pp. 3589–3607).

Nakamura, Y. (2003). New identification of deep moonquakes in the apollo lunar seismic data. *Physics of the Earth and Planetary Interiors*, *139*(3-4), 197–205.

Nakamura, Y. (2005). Spatial extent of a deep moonquake nest–a preliminary report of reexamination. In *36th annual lunar and planetary science conference* (p. 1168).

Nunn, C., Garcia, R. F., Nakamura, Y., Marusiak, A. G., Kawamura, T., Sun, D., ... others (2020). Lunar seismology: a data and instrumentation review. *Space Science Reviews*, *216*(5), 1–39.

Nunn, C., Nakamura, Y., & Igel, H. (2017). Apollo passive seismic experiments: lunar data in seed format. In *Agu fall meeting abstracts* (Vol. 2017, pp. P41D–2860).

Nunn, C., Weber, R. C., & Panning, M. (2020). Improving the accessibility of the apollo seismic data: Archiving at iris and the pds. In *Lunar and planetary science conference* (p. 2269).

Ogawa, M. (1987). Shear instability in a viscoelastic material as the cause of deep focus earthquakes. *Journal of Geophysical Research: Solid Earth*, *92*(B13), 13801-10.

Proctor, B., & Hirth, G. (2015). Role of pore fluid pressure on transient strength changes and fabric development during serpentine dehydration at mantle conditions: Implications for subduction-zone seismicity. *Earth and Planetary Science Letters*, *421*, 1–12.

Qin, C., Muirhead, A. C., & Zhong, S. (2012). Correlation of deep moonquakes and mare basalts: Implications for lunar mantle structure and evolution. *Icarus*, *220*(1), 100–105. doi: 10.1016/j.icarus.2012.04.023

Sakamaki, T., Ohtani, E., Urakawa, S., Suzuki, A., Katayama, Y., & Zhao, D. (2010). Density of high-ti basalt magma at high pressure and origin of heterogeneities in the lunar mantle. *Earth and Planetary Science Letters*, *299*(3-4), 285–289.

Schubnel, A., Brunet, F., Hilairet, N., Gasc, J., Wang, Y., & Green, H. W. (2013). Deep-focus earthquake analogs recorded at high pressure and temperature in the laboratory. *Science*, *341*(6152), 1377–1380.

Solomon, S., & Chaiken, J. (1976). Thermal expansion and thermal stress in the moon and terrestrial planets-clues to early thermal history. In *Lunar and planetary science conference proceedings* (Vol. 7, pp. 3229–3243).

Steinberger, B., Zhao, D., & Werner, S. C. (2015). Interior structure of the moon: constraints from seismic tomography, gravity and topography. *Physics of the Earth and Planetary Interiors*, *245*, 26–39.

Thielmann, M. (2018). Grain size assisted thermal runaway as a nucleation mechanism for continental mantle earthquakes: Impact of complex rheologies. *Tectonophysics*, *746*, 611–623.

Thielmann, M., Rozel, A., Kaus, B., & Ricard, Y. (2015). Intermediate-depth earthquake generation and shear zone formation caused by grain size reduction and shear heating. *Geology*, *43*(9), 791–794.

Toksöz, M. N., Goins, N. R., & Cheng, C. (1977). Moonquakes: Mechanisms and relation to tidal stresses. *Science*, *196*(4293), 979–981.

Weber, R. C., Bills, B., & Johnson, C. (2009). Constraints on deep moonquake focal mechanisms through analyses of tidal stress. *Journal of Geophysical Research: Planets*, *114*(E5).

Weber, R. C., Bills, B. G., & Johnson, C. L. (2010). A simple physical model for deep moonquake occurrence times. *Physics of the Earth and Planetary Interiors*, *182*(3-4), 152–160. doi: 10.1016/j.pepi.2010.07.009

White, R. S., Drew, J., Martens, H. R., Key, J., Soosalu, H., & Jakobsdóttir, S. S. (2011). Dynamics of dyke intrusion in the mid-crust of iceland. *Earth and Planetary Science Letters*, *304*(3-4), 300–312.

Yang, W., Hauksson, E., & Shearer, P. M. (2012). Computing a large refined catalog of focal mechanisms for southern california (1981–2010): Temporal stability of the style of faulting. *Bulletin of the Seismological Society of America*, *102*(3), 1179–1194.

Zhao, D., Arai, T., Liu, L., & Ohtani, E. (2012). Seismic tomography and geochemical evidence for lunar mantle heterogeneity: comparing with earth. *Global and Planetary Change*, *90*, 29–36.

JOURNAL OF GEOPHYSICAL RESEARCH

Supporting Information for Stresses in the lunar interior: insights from slip directions in the A01 deep moonquake nest

A. R. Turner [1], J.C. Hawthorne [1]and M. Gaddes [2]

[1]Department of Earth Sciences, University of Oxford, Oxford, UK

[2]COMET, University of Leeds, Leeds, UK

Contents of this file

1. Figures s.1 to s.29

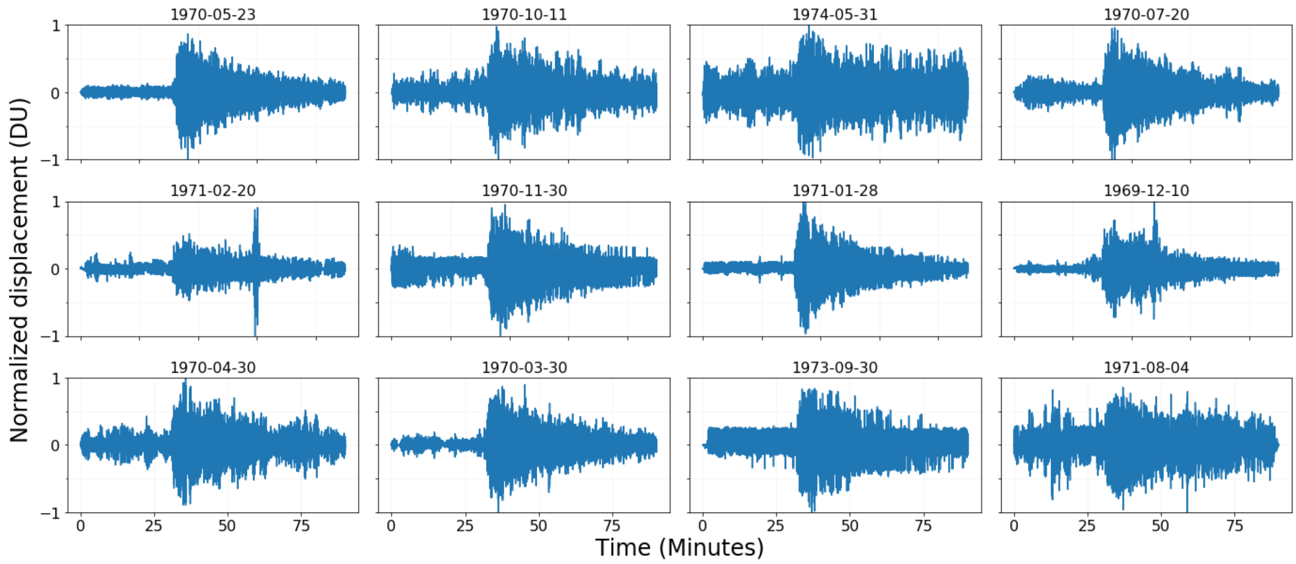

Figure S1. Deep moonquake waveforms used for PCA decomposition, recorded at station S12, channel MHE, in the peaked operation mode.

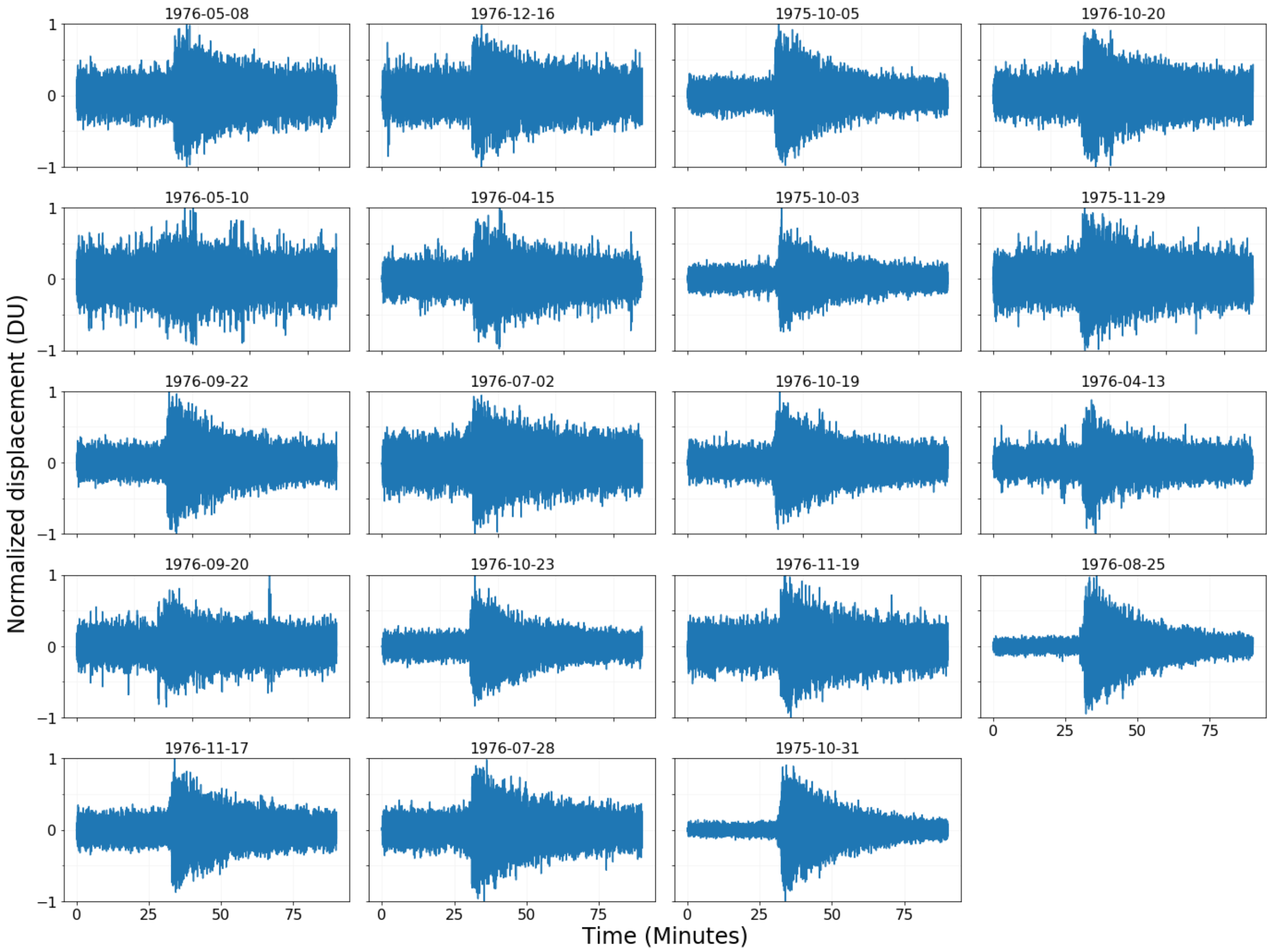

Figure S2. Deep moonquake waveforms used for PCA decomposition, recorded at station S12, channel MHN, in the flat operation mode.

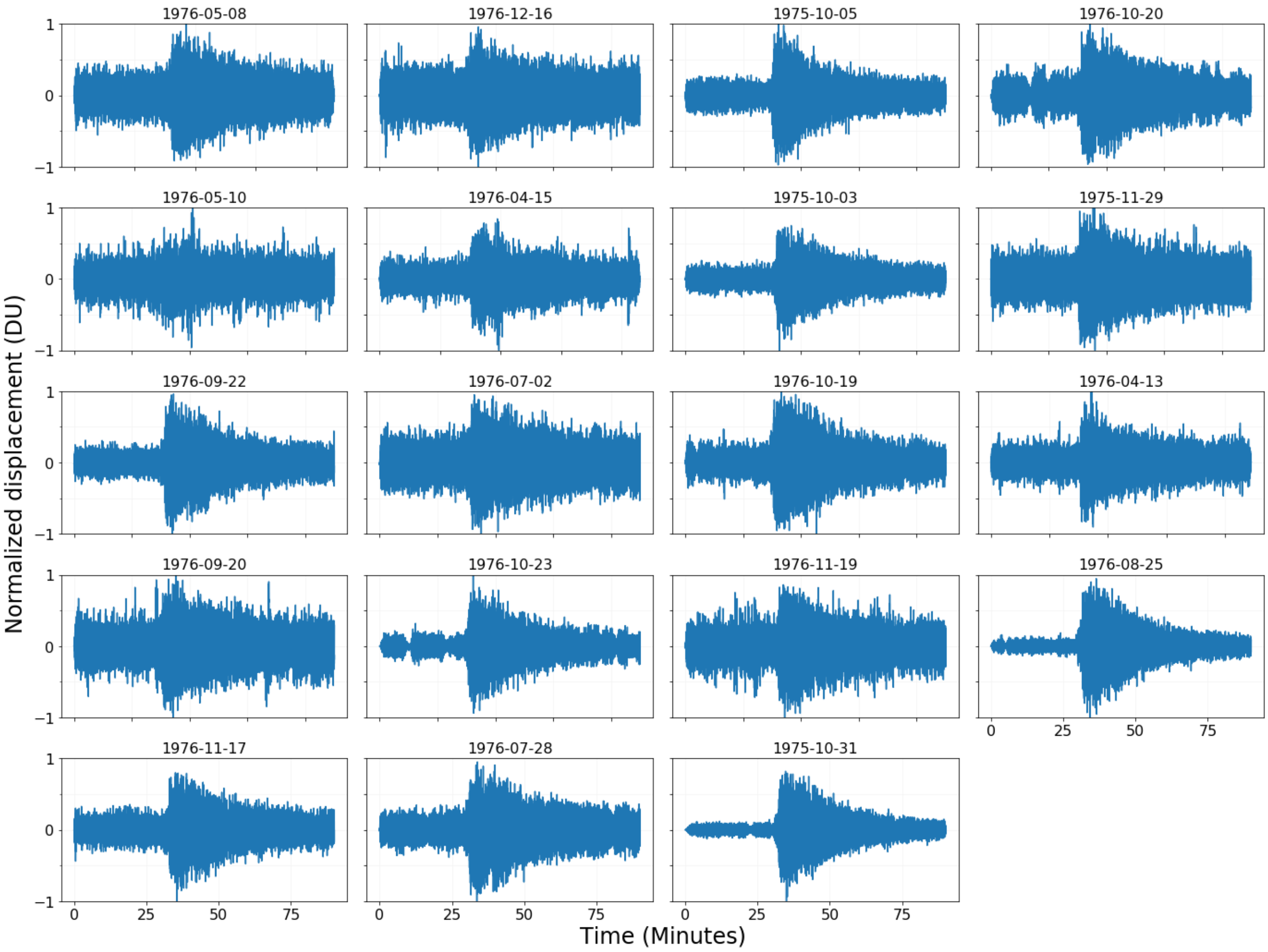

Figure S3. Deep moonquake waveforms used for PCA decomposition, recorded at station S12, channel MHE, in the flat operation mode.

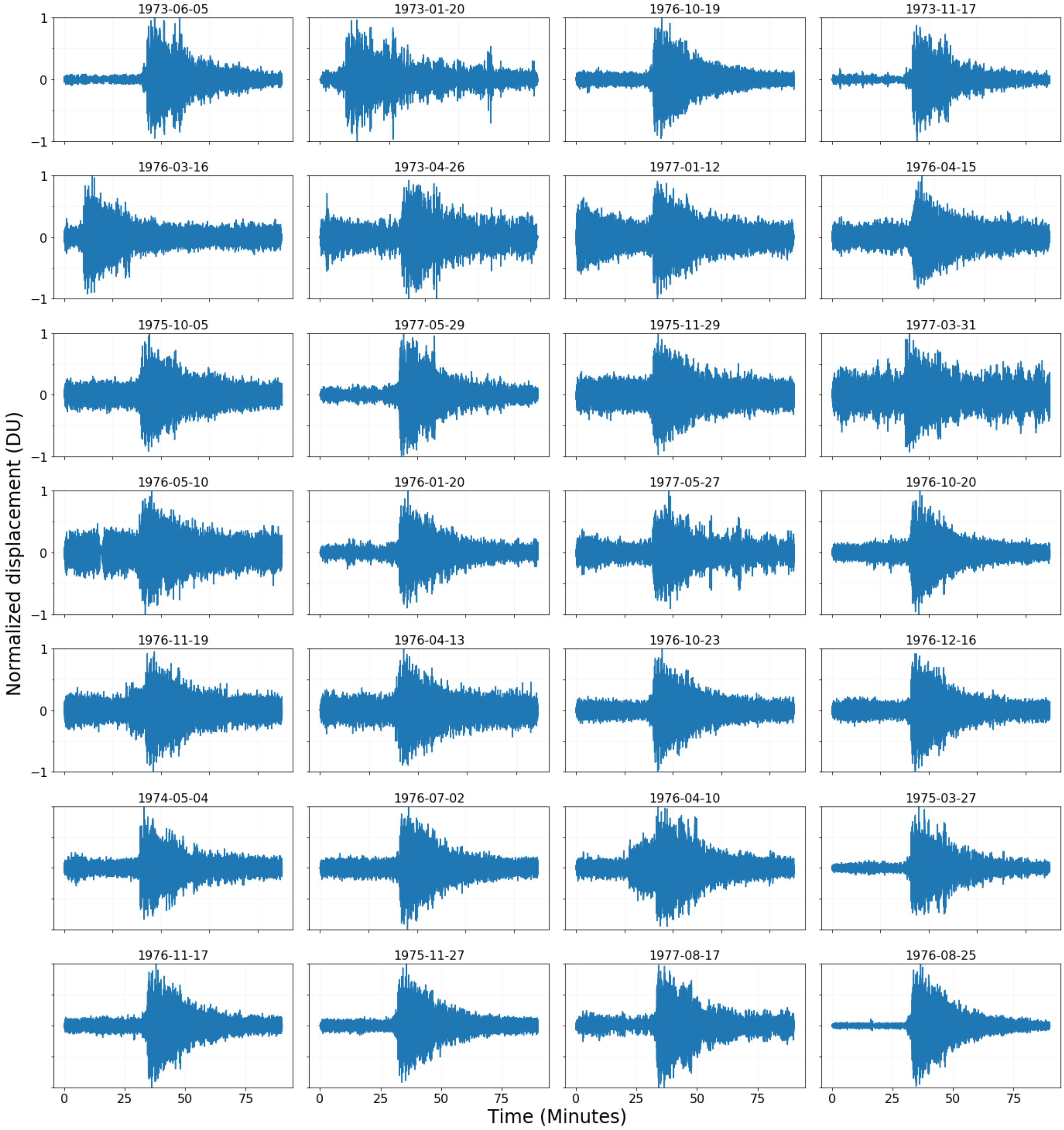

Figure S4. Deep moonquake waveforms used for PCA decomposition, recorded at station S16, channel MHN, in the peaked operation mode.

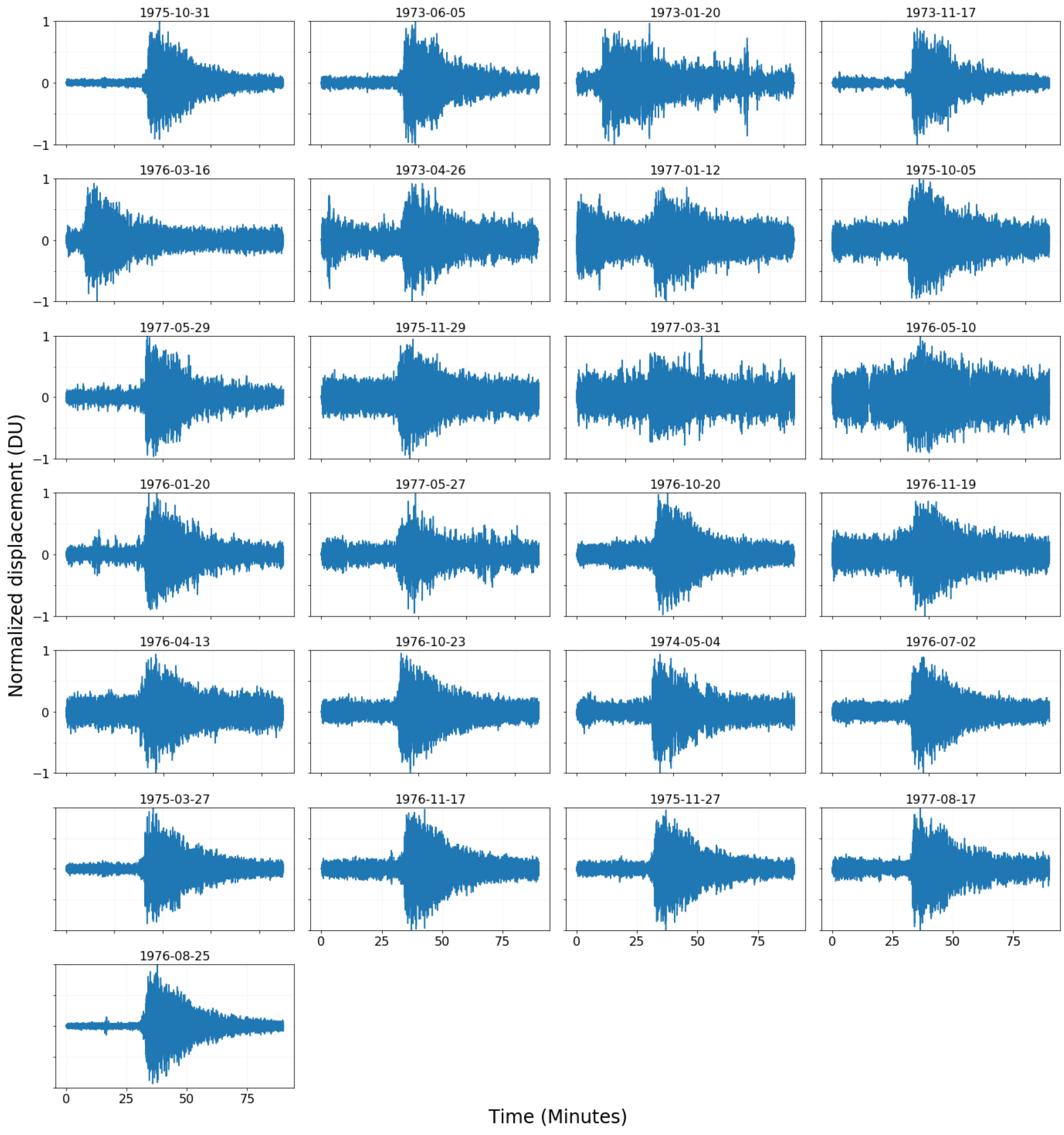

Figure S5. Deep moonquake waveforms used for PCA decomposition, recorded at station S16, channel MHE, in the peaked operation mode.

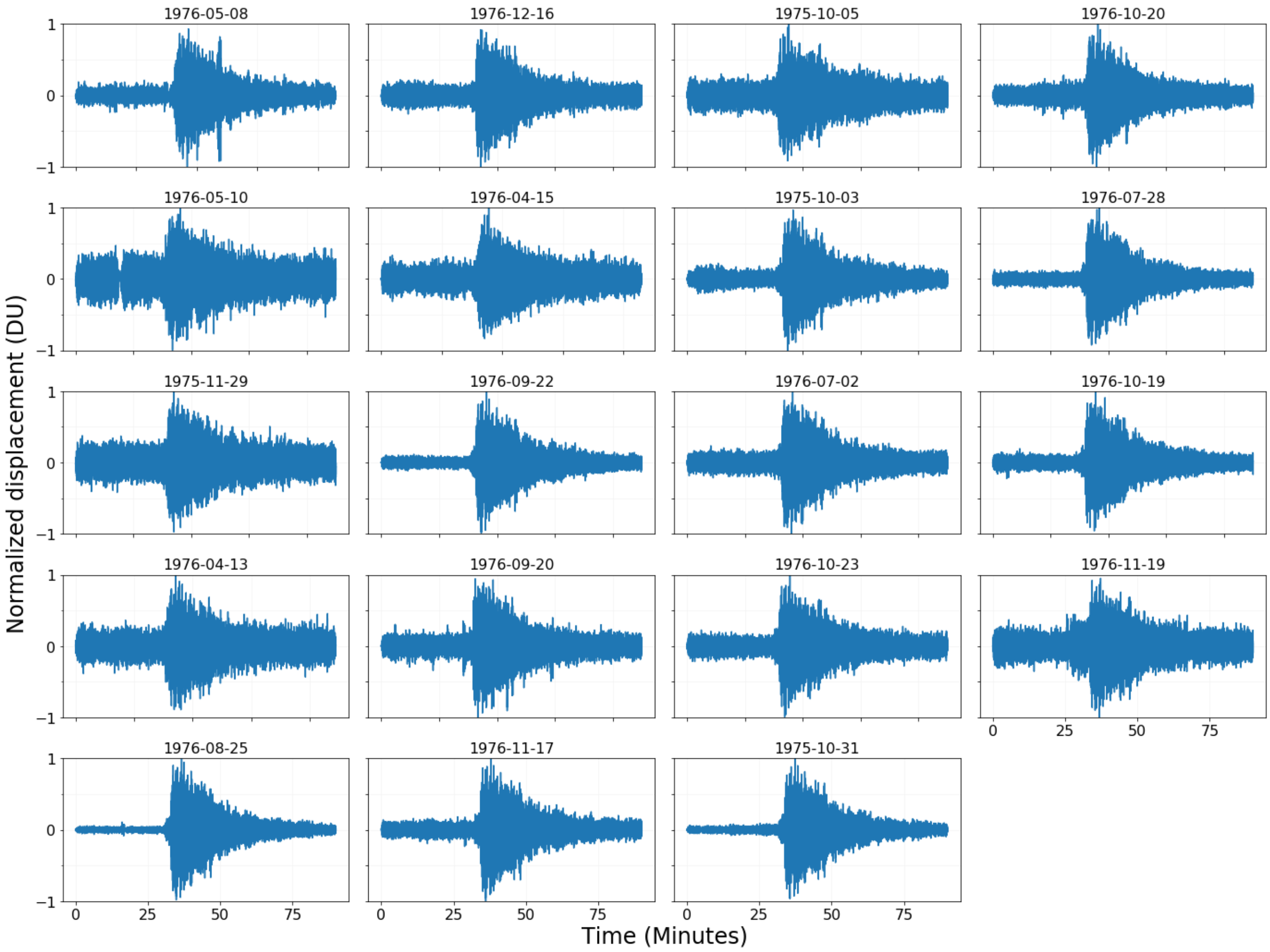

Figure S6. Deep moonquake waveforms used for PCA decomposition, recorded at station S16, channel MHN, in the flat operation mode.

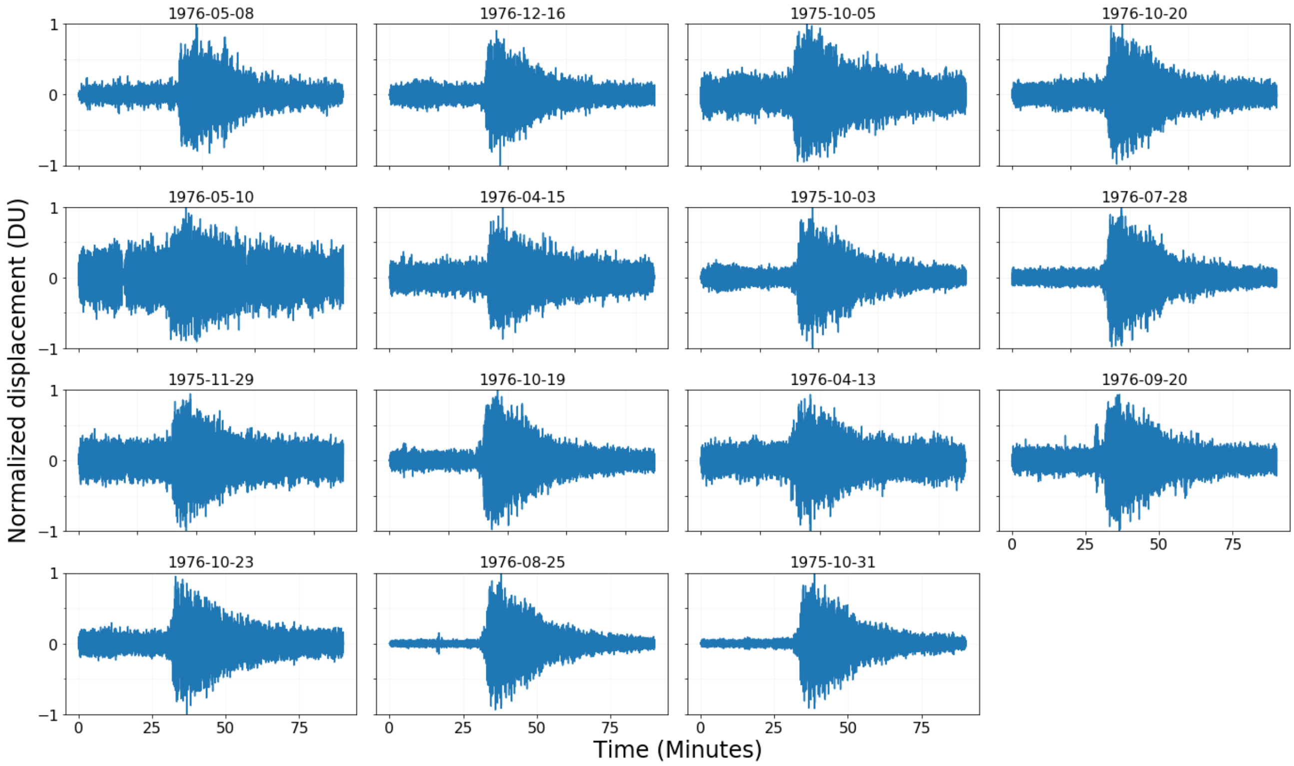

Figure S7. Deep moonquake waveforms used for PCA decomposition, recorded at station S16, channel MHE, in the flat operation mode.

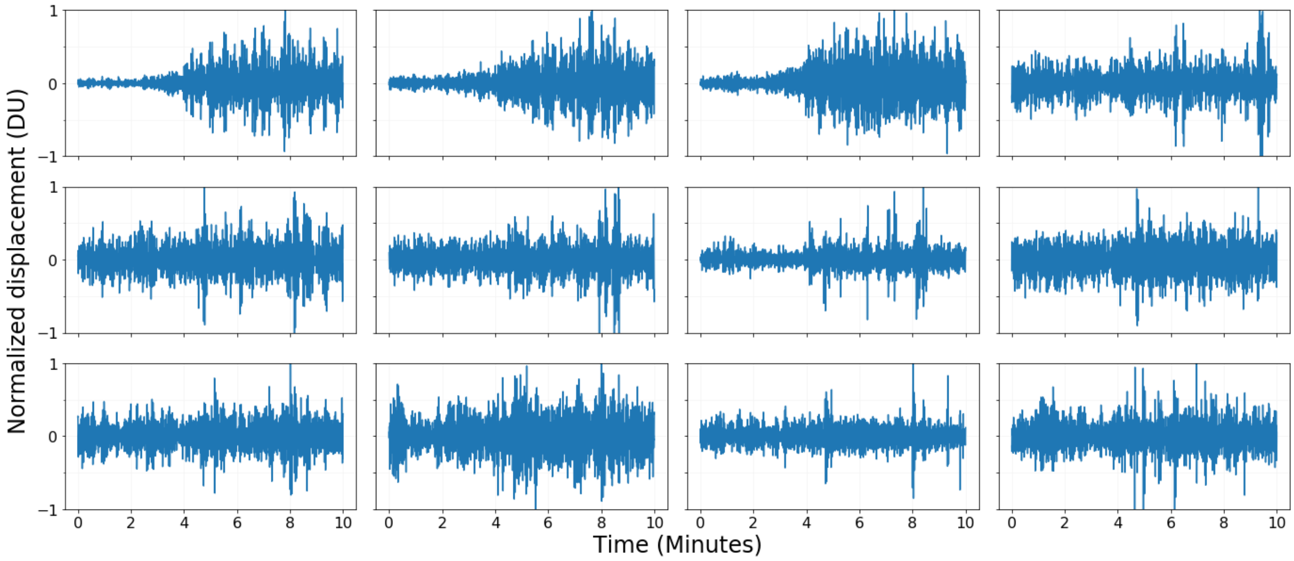

Figure S8. Principal components derived from the S12 MHE data in the peaked operational mode of the instrument.

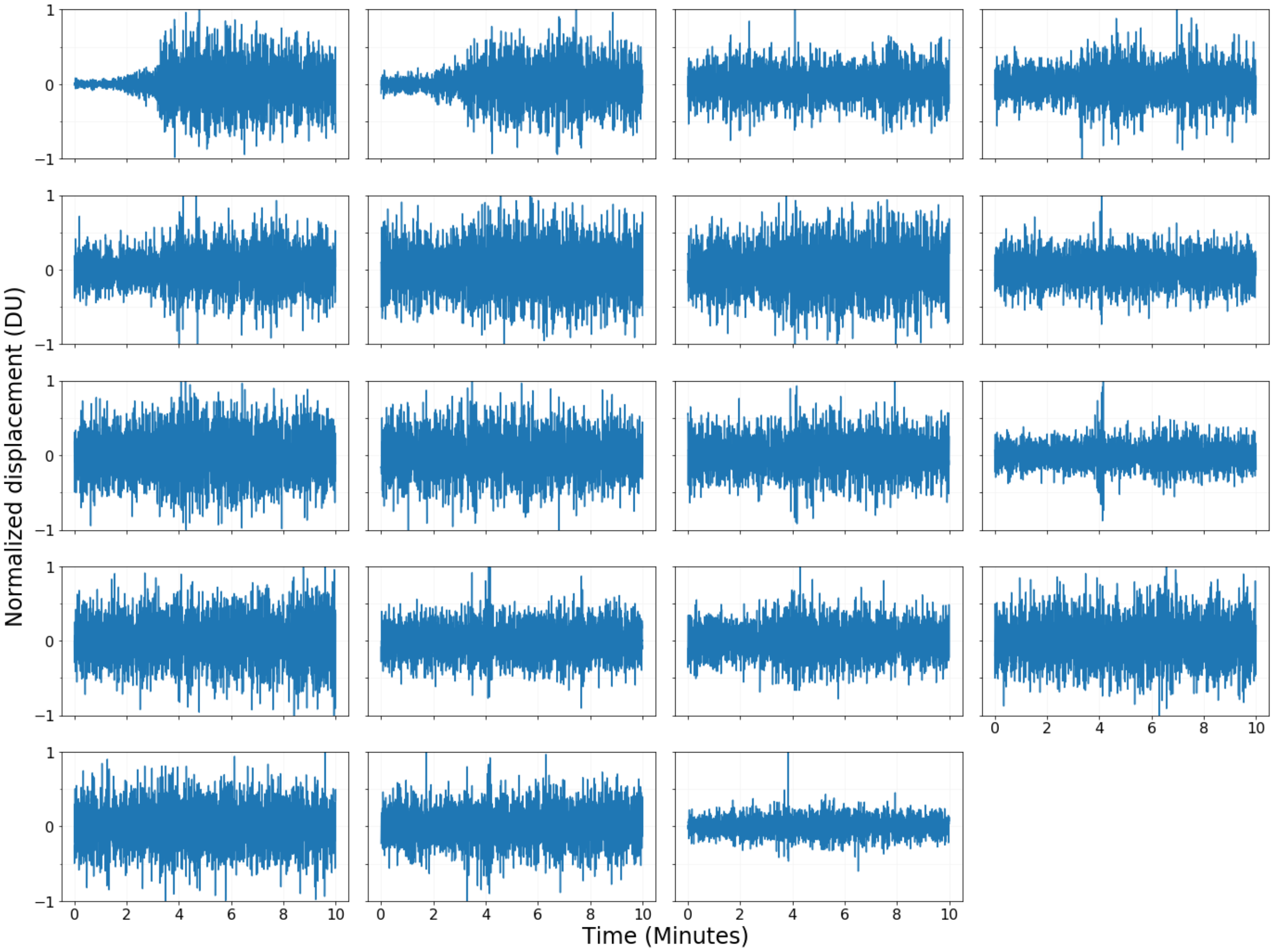

Figure S9. Principal components derived from the S12 MHN data in the flat operational mode of the instrument.

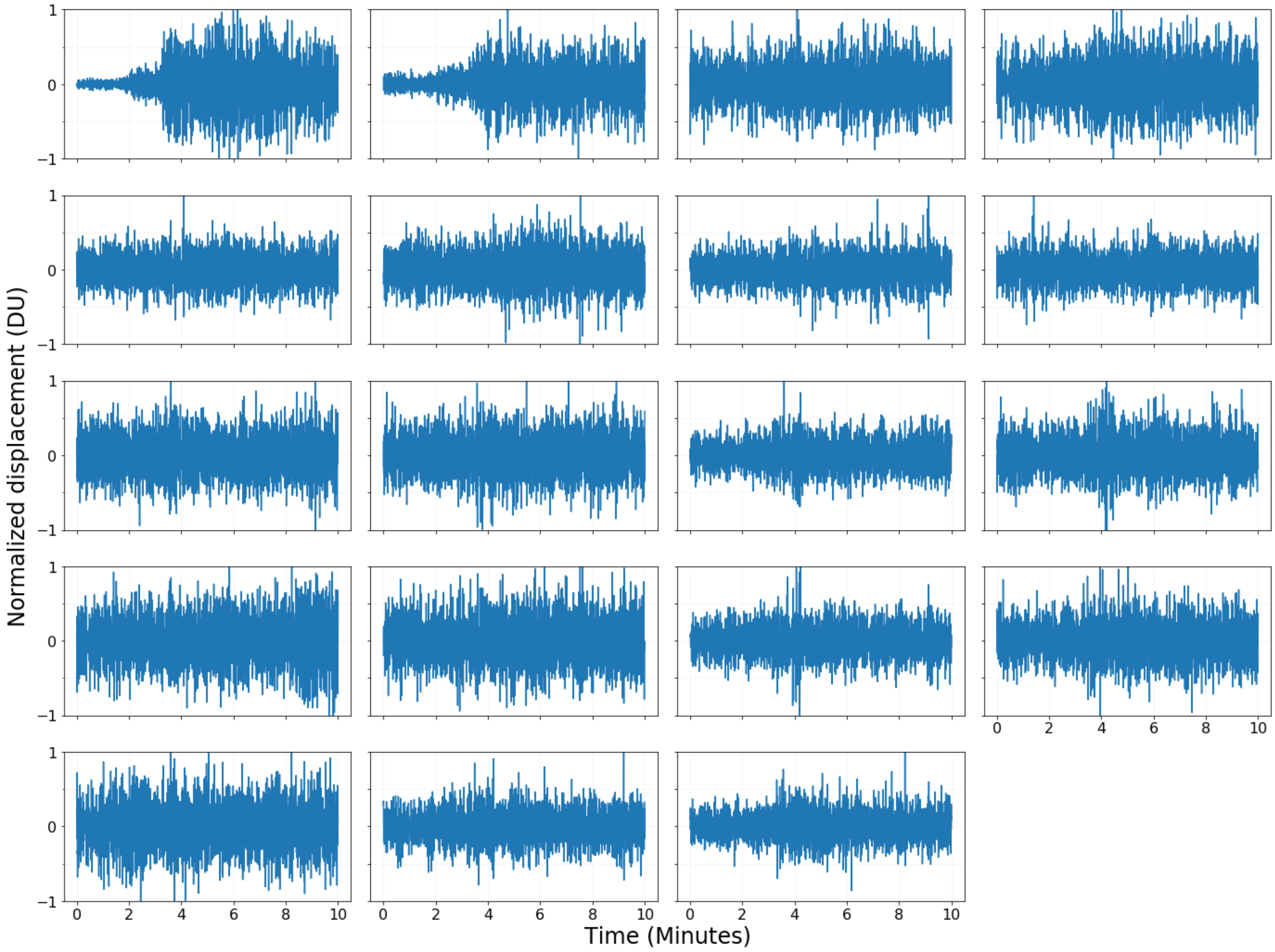

Figure S10. Principal components derived from the S12 MHE data in the flat operational mode of the instrument.

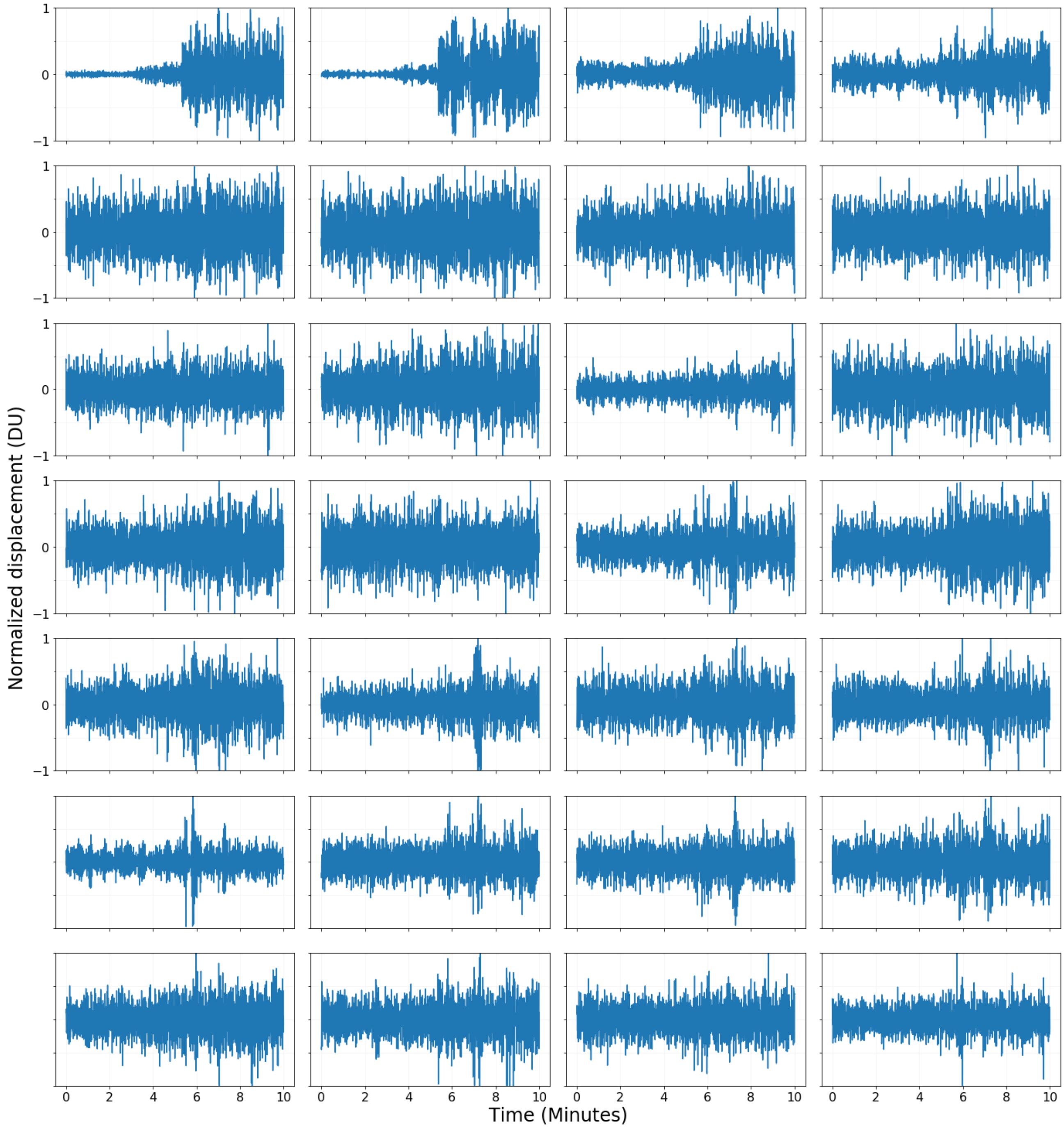

Figure S11. Principal components derived from the S16 MHN data in the peaked operational mode of the instrument.

Figure S12. Principal components derived from the S16 MHE data in the peaked operational mode of the instrument.

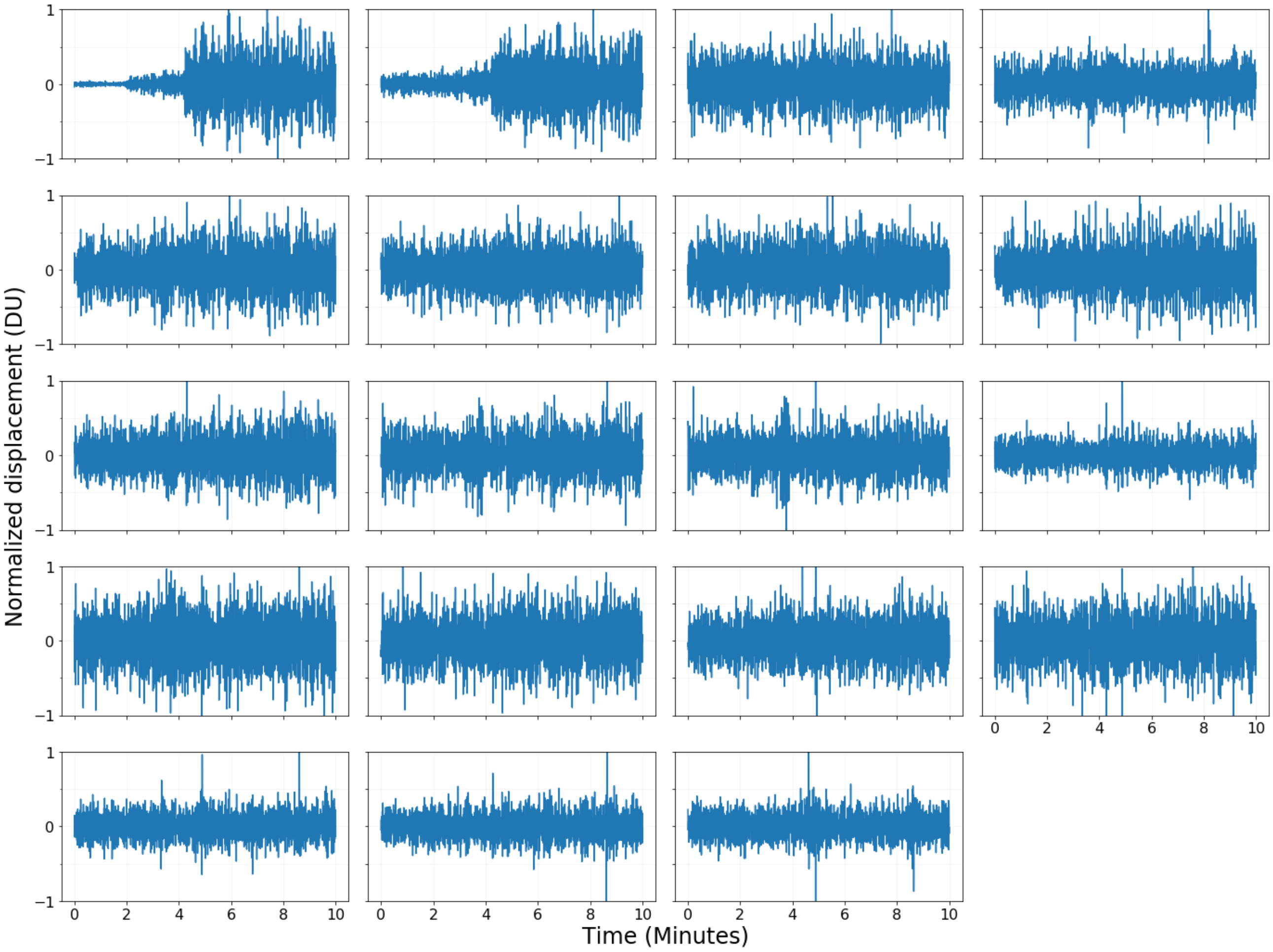

Figure S13. Principal components derived from the S16 MHN data in the flat operational mode of the instrument.

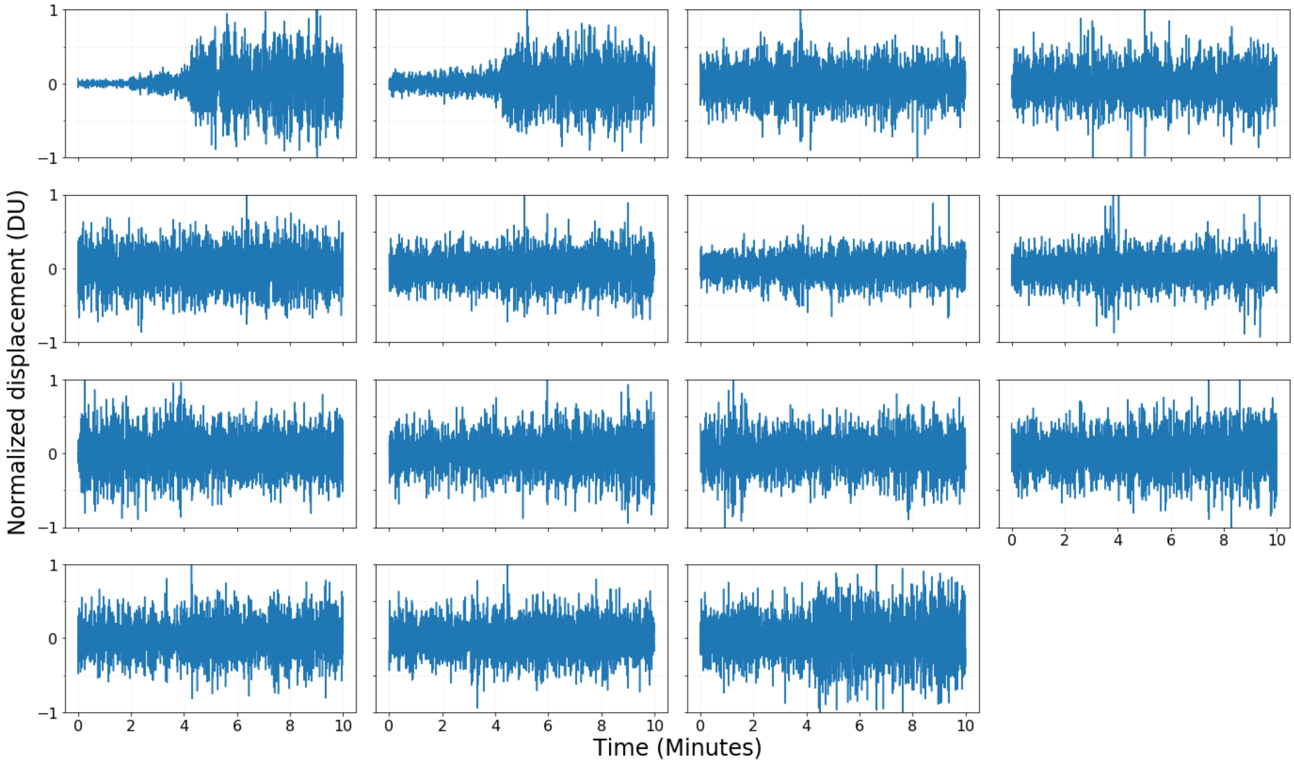

Figure S14. Principal components derived from the S16 MHE data in the flat operational mode of the instrument.

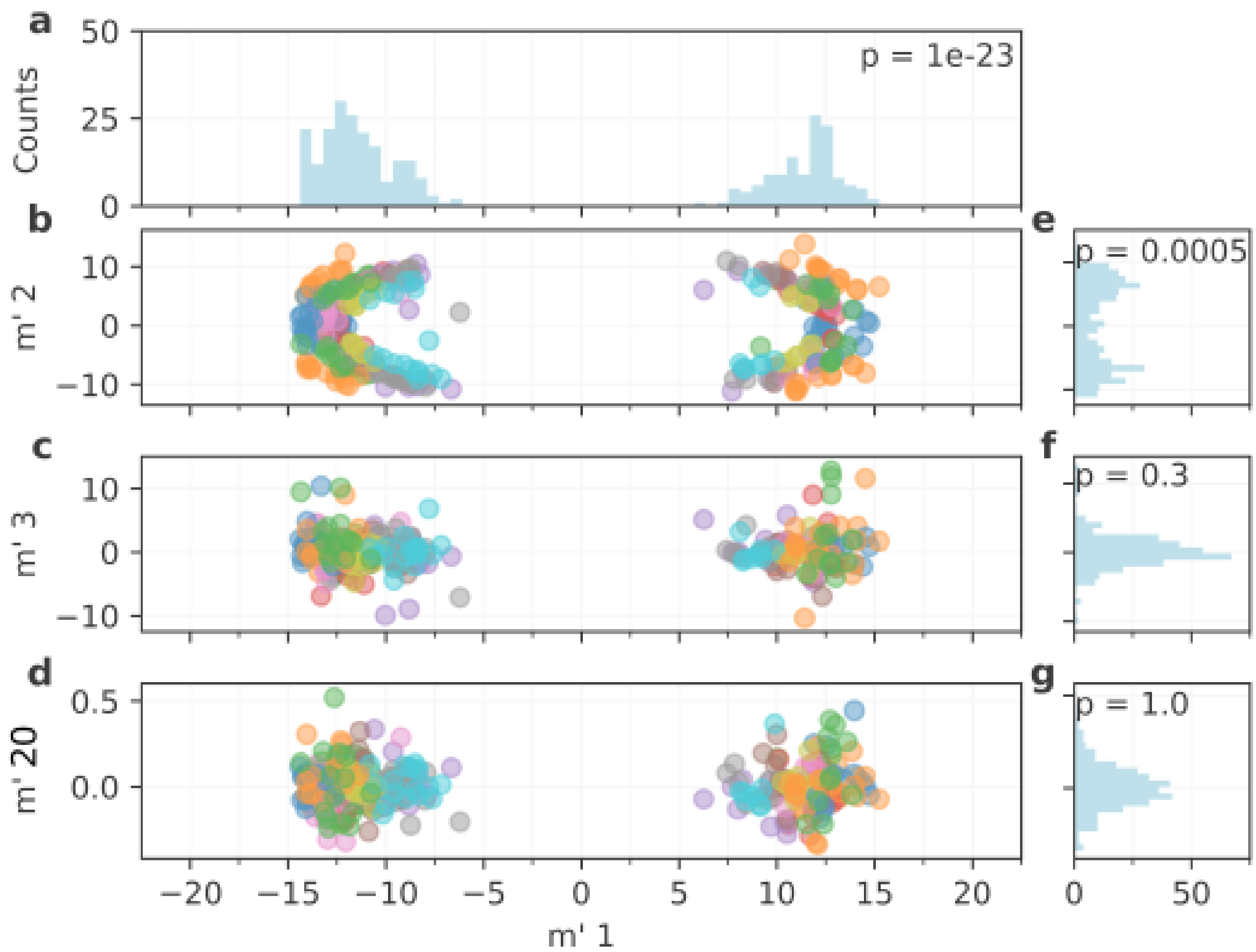

Figure S15. Unbiased coefficients of the principal components, from the S12 MHE data in the peaked operational mode. In panels b-d, the coefficient for the first principal component m'_{i1} is plotted on the x-axis. The coefficients of the second (m'_2), third (m'_3) and twentieth (m'_{20}) principal components are plotted on the y axis of panels b,c and d, respectively. Each event is plotted in a different colour. Panels a, e, f, and g summarise the distribution of coefficients for each of the principal components. The text in the top of panels a, e, f, and g is the probability (p-value) that each distribution differs from the distribution of the coefficients derived from noise. Only the first two components differ from noise.

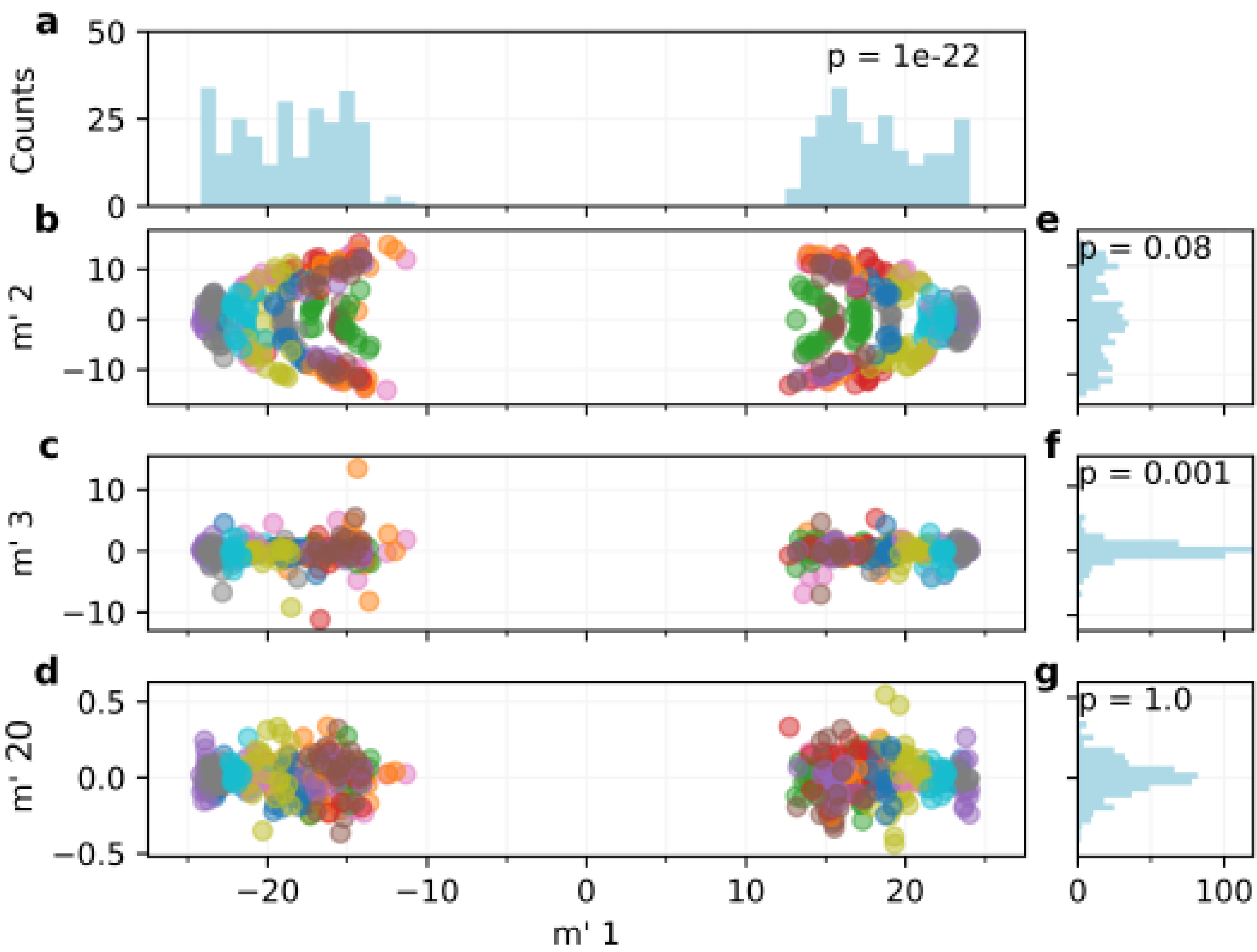

Figure S16. Same as Figure S15 from the S12 MHN data in the flat operational mode.

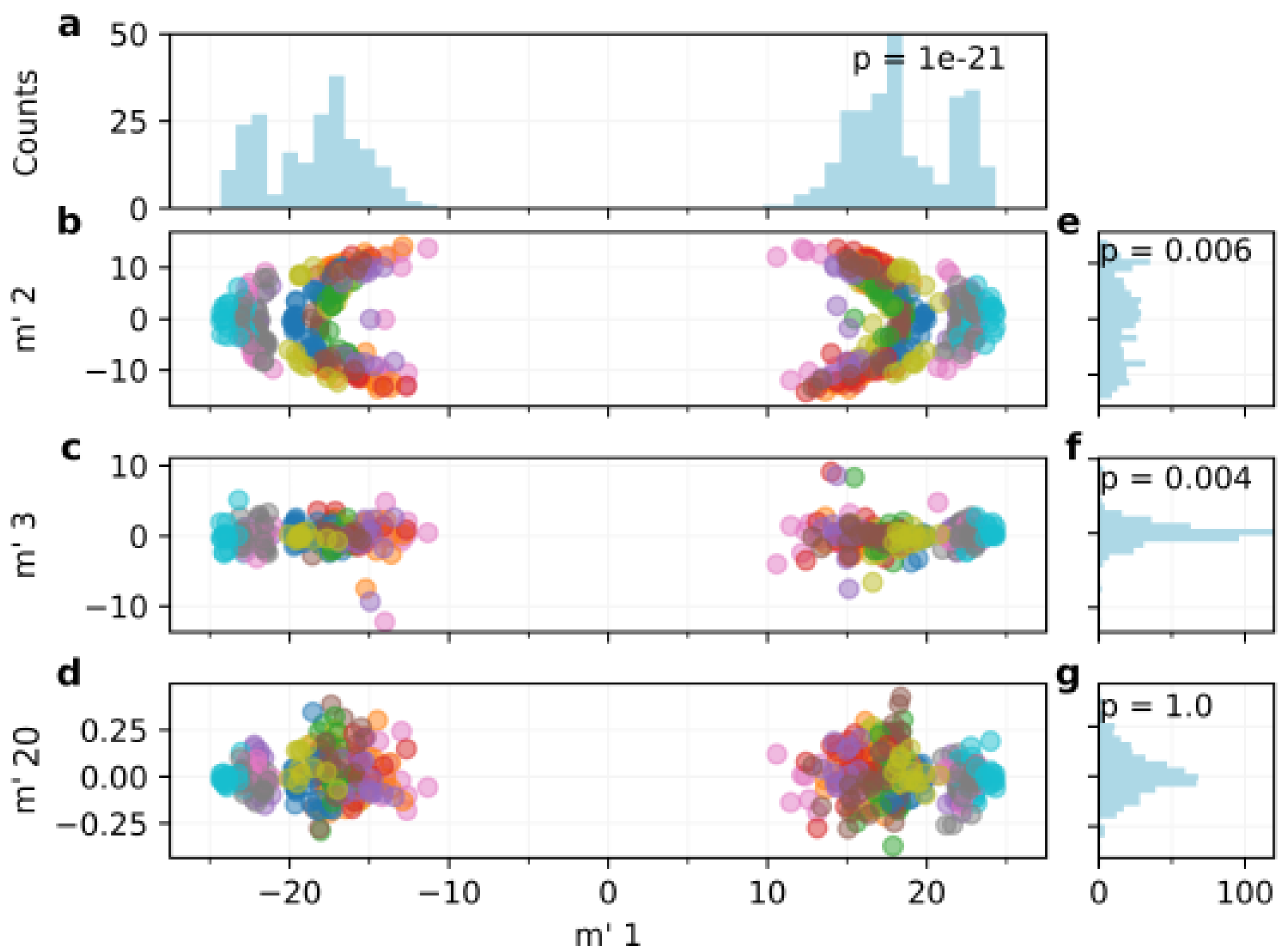

Figure S17. Same as Figure S15 from the S12 MHE data in the flat operational mode.

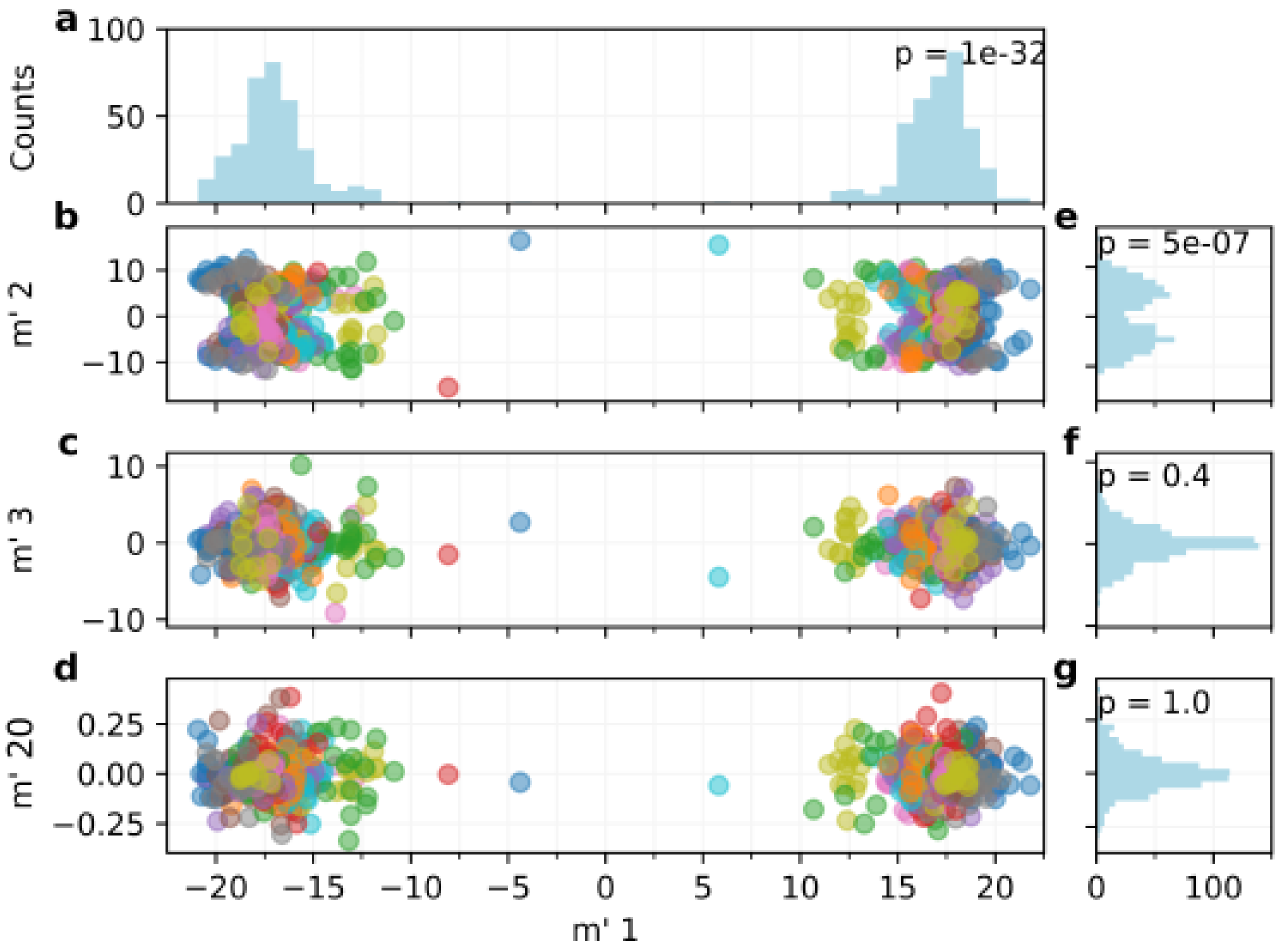

Figure S18. Same as Figure S15 from the S16 MHN data in the peaked operational mode.

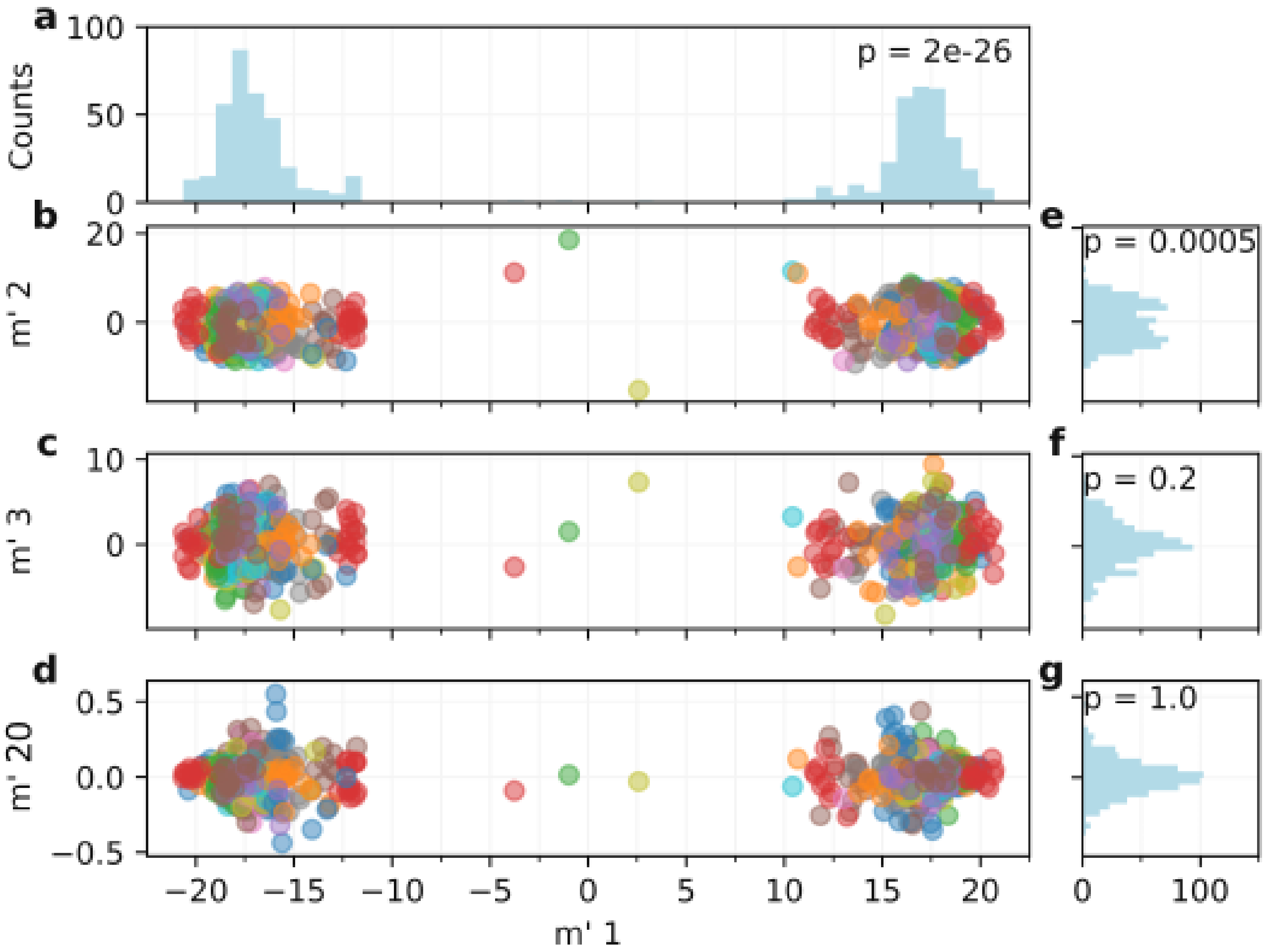

Figure S19. Same as Figure S15 from the S16 MHE data in the peaked operational mode.

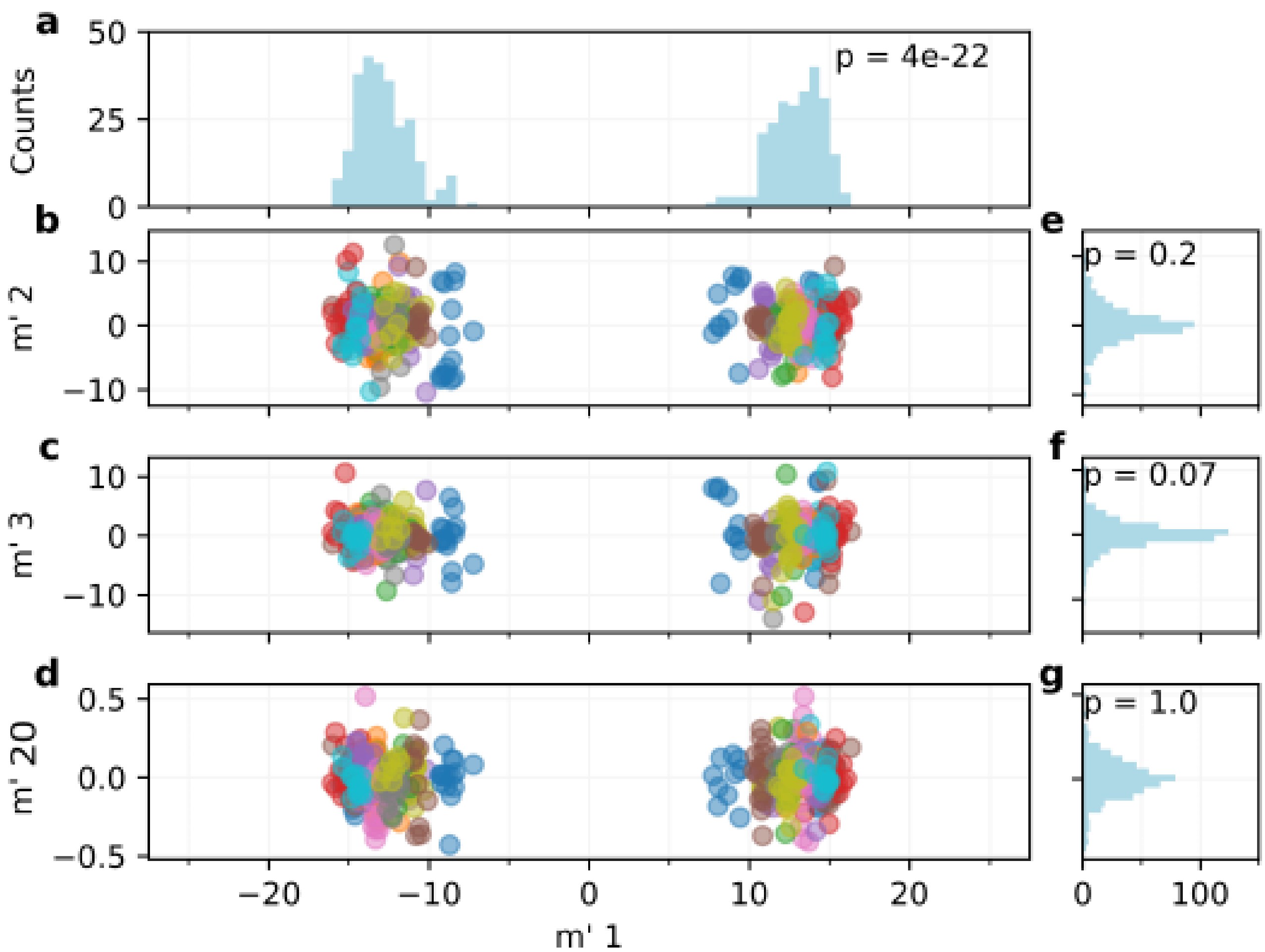

Figure S20. Same as Figure S15 from the S16 MHN data in the flat operational mode.

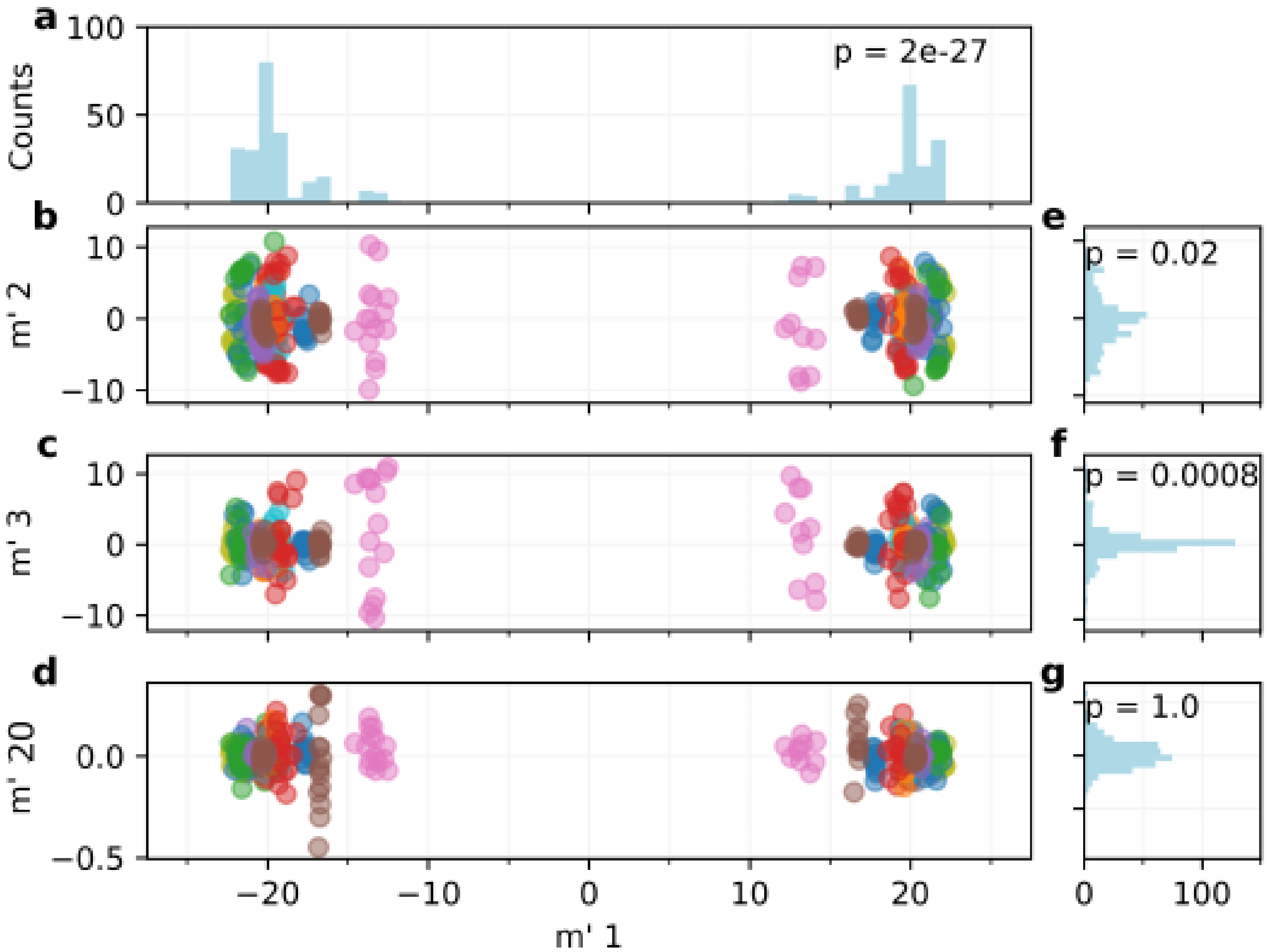

Figure S21. Same as Figure S15 from the S16 MHE data in the flat operational mode.

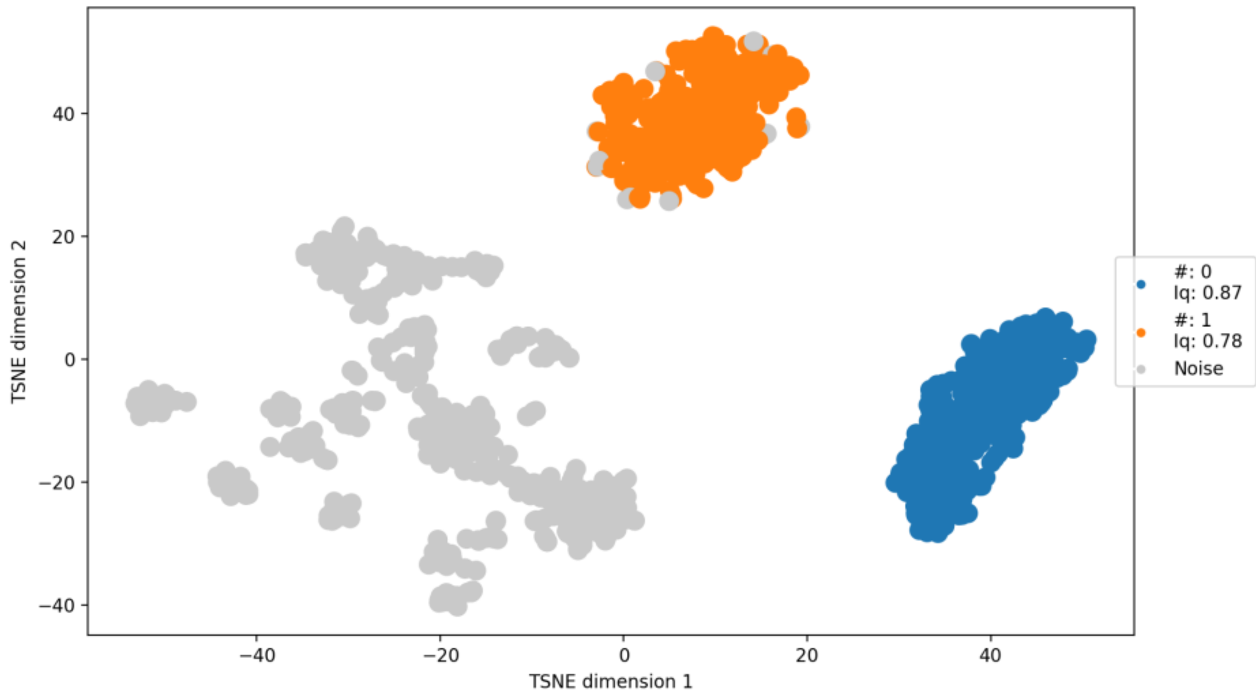

Figure S22. Clustering results of bootstrapped **G**, obtained for S12 MHE in peaked operational mode. One point is plotted for each bootstrapped estimate of a principal component, but only the first four principal components are plotted. The location of each point is determined by the t-sne algorithm, preserving the similarity of components from the higher dimensional space (Maaten Hinton, 2008; Gaddes et al., 2019). The colour of each point is determined by the HBDSCAN clustering algorithm (McInnes et al., 2017; Gaddes et al., 2019). Grey points represent component estimates that are not assigned to a cluster.

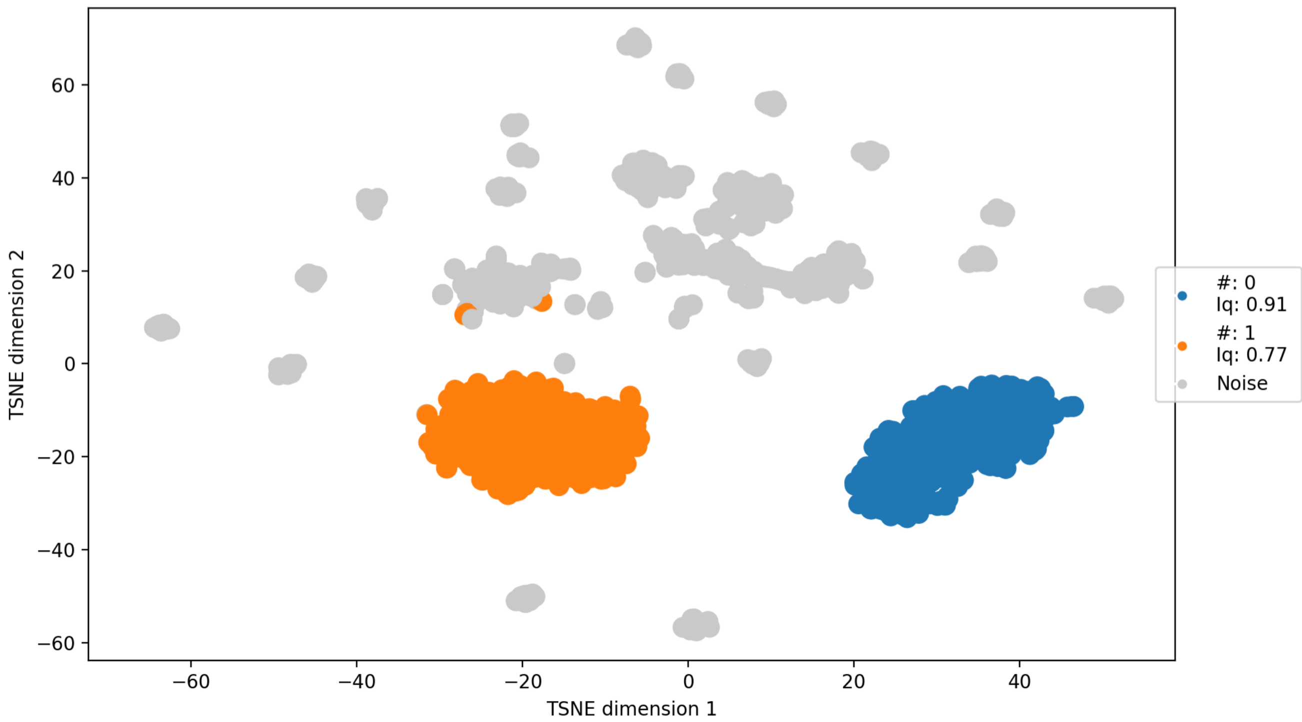

Figure S23. Same as Figure S22 obtained for S12 MHN in flat operational mode.

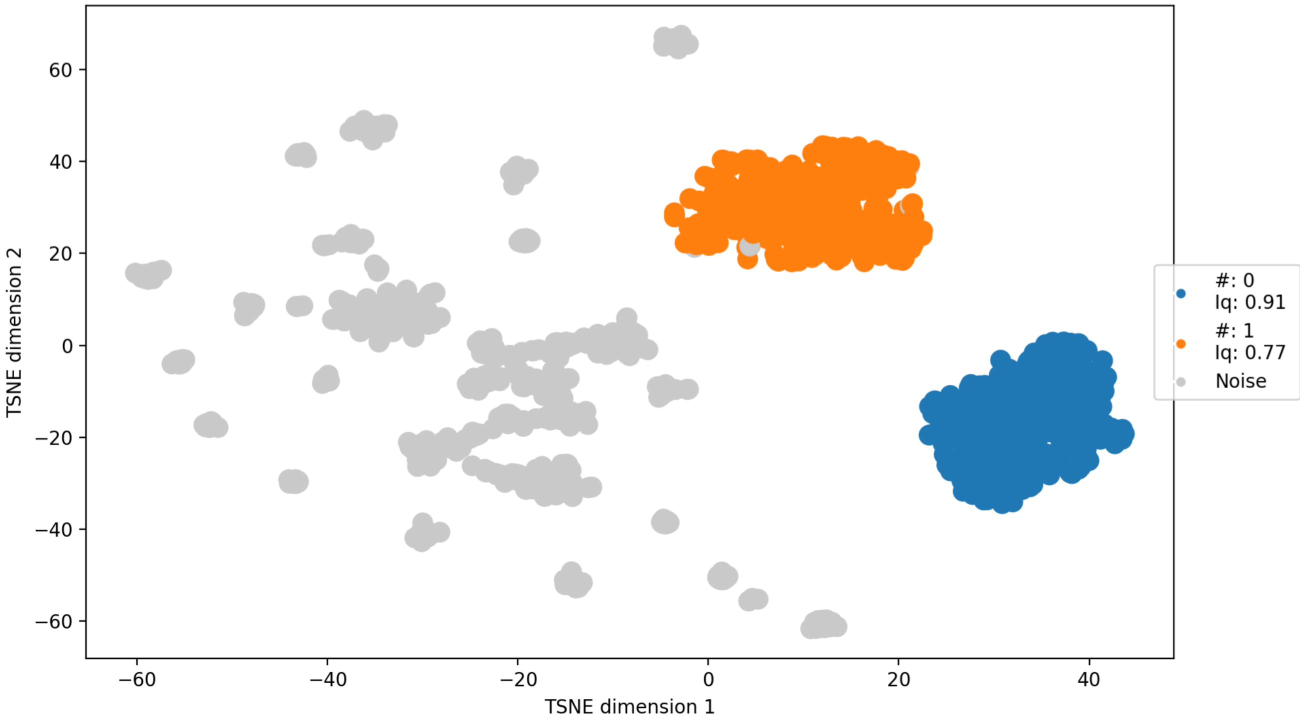

Figure S24. Same as Figure S22 obtained for S12 MHE in flat operational mode.

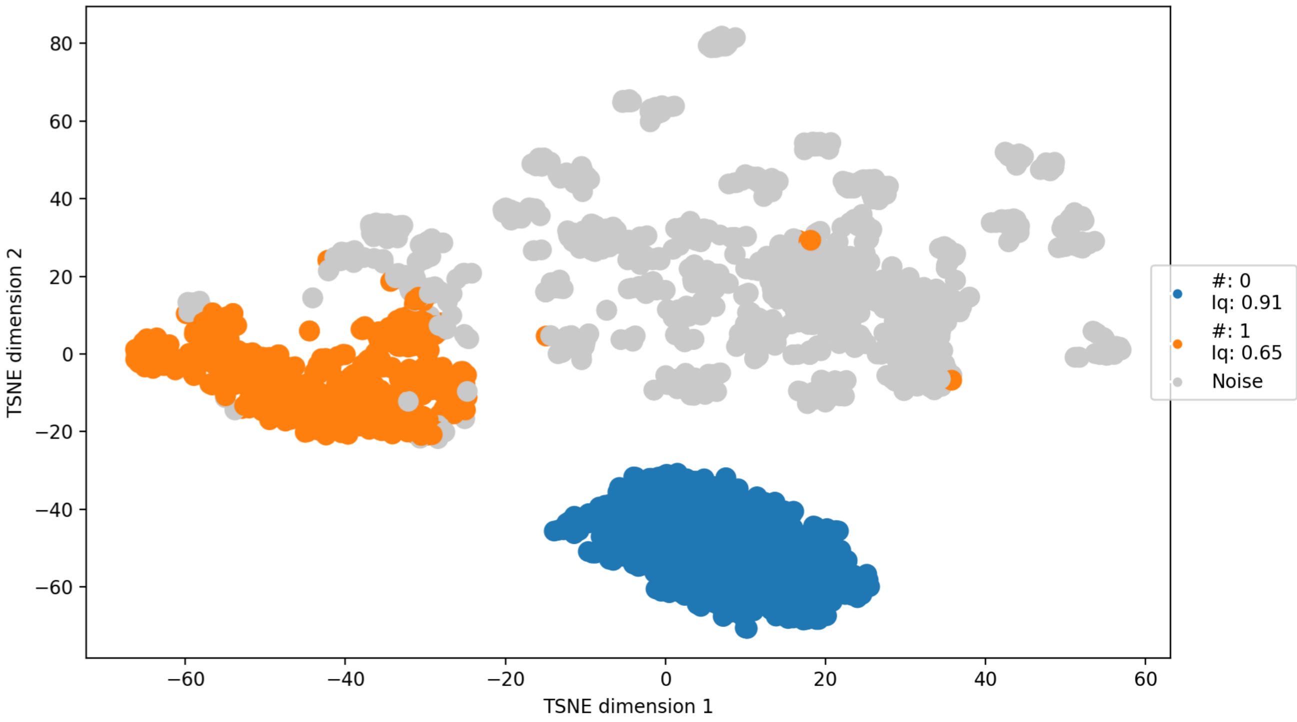

Figure S25. Same as Figure S22 obtained for S16 MHN in peaked operational mode.

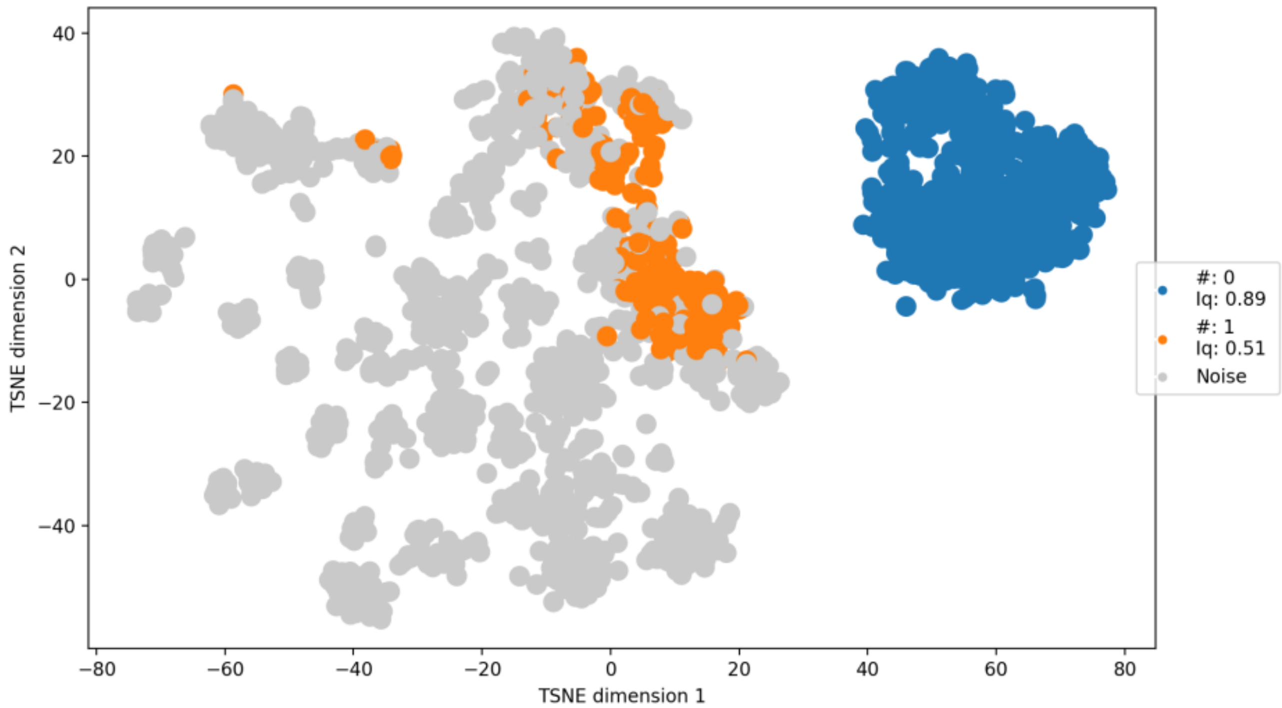

Figure S26. Same as Figure S22 obtained for S16 MHE in peaked operational mode.

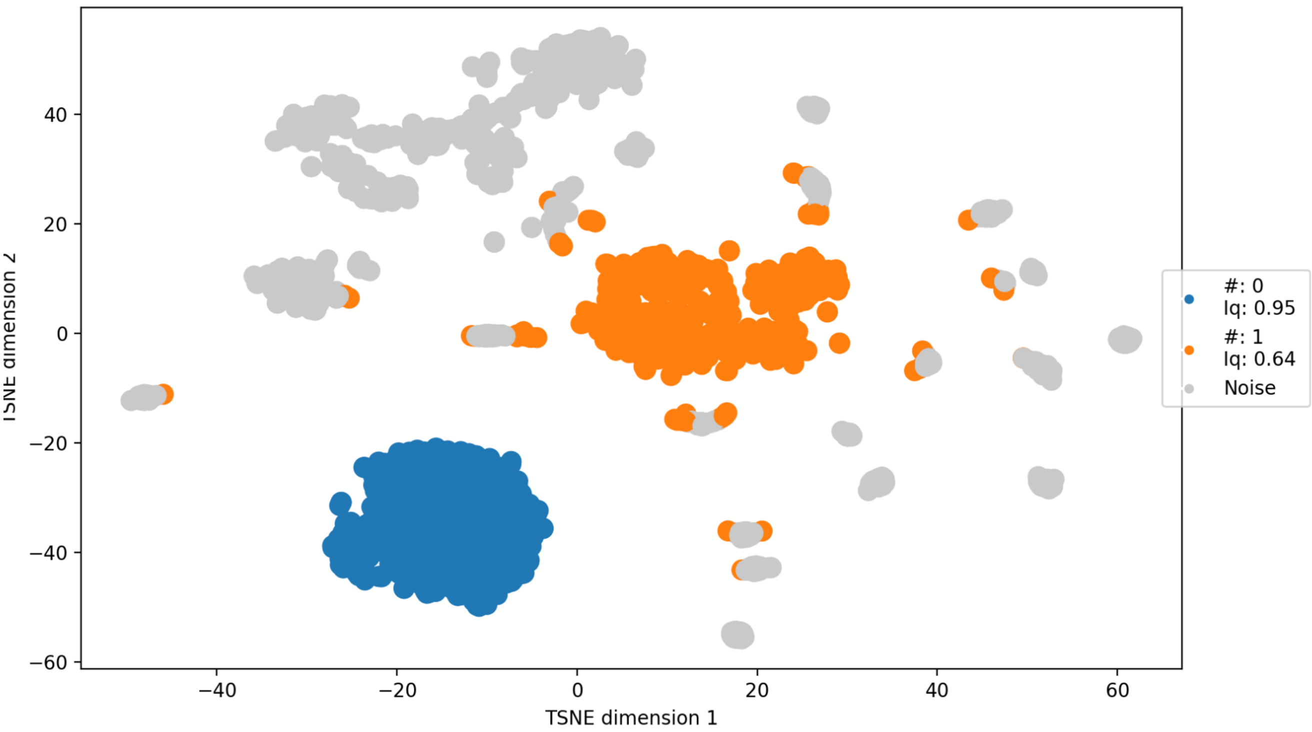

Figure S27. Same as Figure S22 obtained for S16 MHN in flat operational mode.

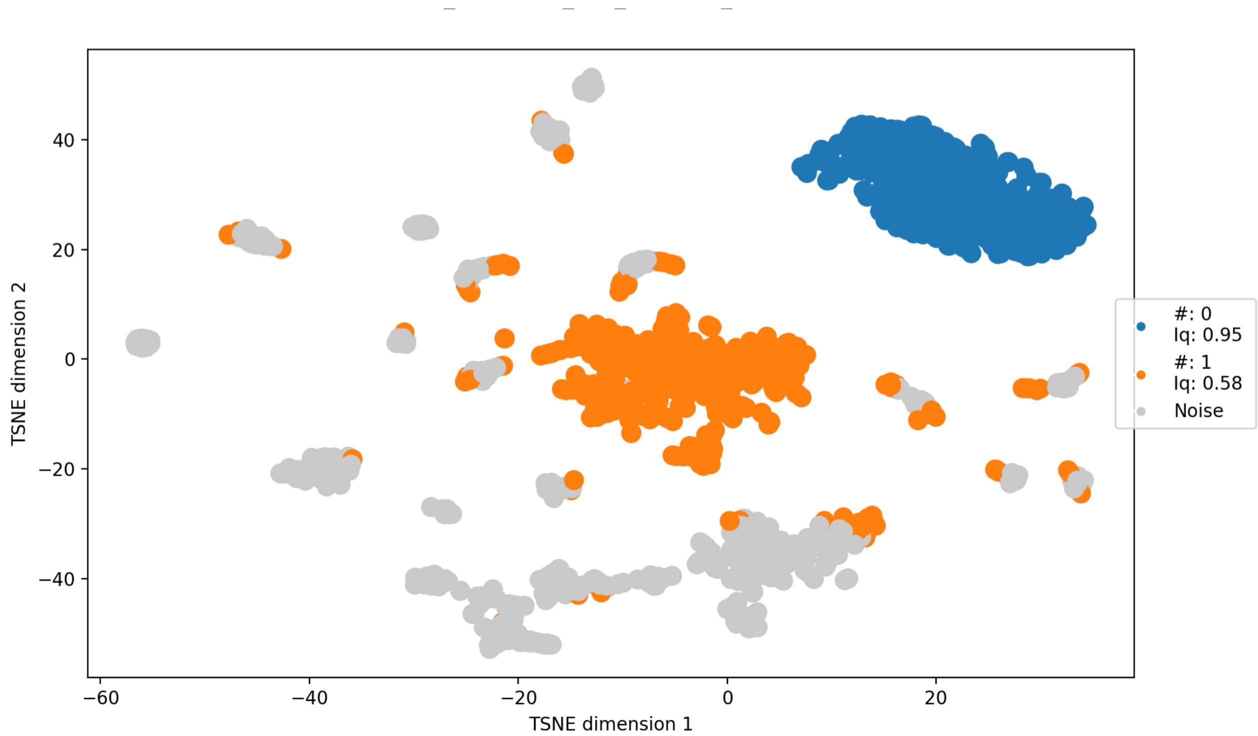

Figure S28. Same as Figure S22 obtained for S16 MHE in flat operational mode.

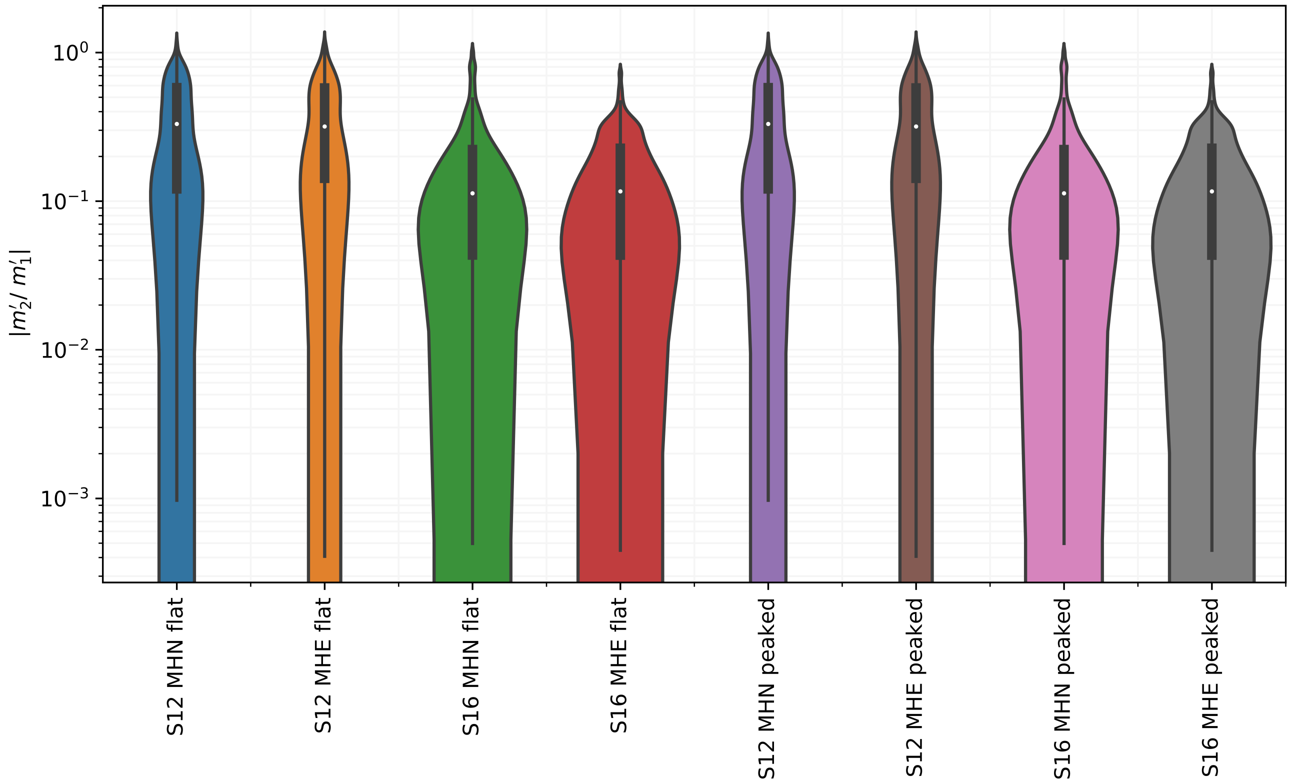

Figure S29. Slip coefficient ratio m_2'/m_1' for each station and channel, now plotted with a log axis. The white dot marks the median bootstrapped ratio at each station, the black bar delimits the interquartile range, and the thin black line delimits 1.5 $\times$ the inter-quartile range. The coloured areas illustrate the probability density of the ratio at each station.